

Observed and predicted Ly α and UV lines for a sample of galaxies at redshifts $z < 3.7$

M. Contini^{1,2}

¹ Dipartimento di Fisica e Astronomia, University of Padova, Vicolo dell'Osservatorio 2. I-35133 Padova, Italy

² School of Physics and Astronomy, Tel Aviv University, Tel Aviv 69978, Israel

Received

ABSTRACT

We explore the origin of the observed Ly α and other UV lines from galaxies at $z < 3.7$ by detailed modelling of the spectra. The objects are chosen among those showing a) UV - optical - near-IR lines, b) only UV lines and c) those showing Ly α in the UV and a few optical lines. We also present UV line predictions for a sample of galaxies in the $0.0686 < z < 0.8829$ range. The sample of galaxies including Ly α observations in their spectra does not show peculiar physical conditions of the emitting gas, nor abnormal element abundances. However, the high velocity ($V_s \geq 1000 \text{ km s}^{-1}$) component of the emitting gas is accompanied by relatively low preshock densities ($n_0 \sim 100\text{-}400 \text{ cm}^{-3}$) leading in some cases to broad forbidden lines. Some spectra are best reproduced by shock dominated models in which the photoionizing source is hidden or absent. Within more than 50 galaxies modelled in this work, only a few spectra from galaxies at $z \geq 2.5$ correspond to a starburst temperature $T_* > 10^5 \text{ K}$, similar to that found in galaxies showing some activity.

Key words. radiation mechanisms: general — shock waves — ISM: abundances — galaxies: Seyfert — galaxies: starburst — galaxies: high redshift

1. Introduction

Ly α is one of the strongest lines in the UV because H is the most abundant element and because corresponding to the 1S-2P transition. Ly α $\lambda 1215$ line in the far-UV is now reported by observations of galaxies at high redshifts (e.g. Humphrey et al 2008, Dawson et al 2003, Stern et al 2002, Erb et al 2010, Fosbury et al 2003, Vernet et al 2000, Dey et al 2005, Norman et al 2002, Finkelstein et al 2011 etc). The line flux is absorbed by dust, depending on the environments of the Ly α emitting nebula. The grains embedded into the gaseous clouds or distributed throughout the photon's way to Earth can lead to a significant drop of the flux (Finkelstein et al 2011). The escape probability was treated by Atek et al (2014) who confirmed that the Ly α escape fraction depends on the dust extinction, but the correlation does not follow the expected curve for a simple dust attenuation. They claim that a higher attenuation can be attributed also to a scattering process and that the strength of Ly α and the escape fraction appear unrelated to the galaxy metallicity.

Supernova (SN) events throughout galaxies lead to specific shocks in the regions surrounding the SN explosion (Heng & Sunyaev 2008) and close to outbursts in novae and symbiotic stars (Contini et al 2009). Heng & Sunyaev (2008) claim that charge transfer reactions between hydrogen atoms and protons in collisionless shocks of SN remnants produce broad Balmer, Lyman, and other hydrogen lines with increased Ly α /H β .

Generally, photoionization by active galactic nuclei (AGN) or by starbursts (SB) is the main heating and ionizing mechanism of gas throughout the galaxy. When no photoionization source is seen, and much of the energy is provided by the conversion of kinetic energy of motion into heat, e.g. when fast moving matter collides with ambient ISM gas, ionization and thermal energy

are released. They will be partly radiated as recombination and collisional line emission (Osterbrock 1989).

It was suggested that high redshift galaxies originate from merging (e.g. Ryan et al 2008). Therefore strong shocks could appear in some regions of the product galaxy, as e.g. in the local galaxy NGC 3393 (Contini 2012). Yajima et al (2012) proposed a formation model from major mergers of gas rich galaxies emitting the Ly α line. They claim that at $z \geq 2$ the merger rate is higher in dense region and the progenitors are more gas rich. Lyman break technique could be employed to explore galaxies at $0.8 \leq z \leq 2.5$ (Oteo et al. 2002). Merging galaxies emit Ly α as well as many other lines. Observations of UV lines are now available from galaxies at high z , in particular NV 1240, CIV 1550, HeII 1640, etc. and eventually OVI 1034. They are emitted by high ionization-level ions that are easily produced in shock heated gas corresponding to suitable velocities. High ionization-level lines are strong from C, N, O, Ne, etc. in the IR, optical, and UV frequency ranges. Most of the UV lines (e.g. OIV, OV, NV) are permitted, while e.g. [NV], [OV], etc in the optical and IR are forbidden and thus collisionally deexcited at high densities.. Permitted lines originate from recombination and depend on radiative processes. Both radiation and collisional processes should be considered in the calculation of line spectra rich enough to constrain the models. Composite models (shock +photoionization) were adopted to explain the spectra from local merging galaxies (e.g. NGC 7212, NGC 3393, NGC 6240, Arp 220, Contini 2013a and references therein) and were used in the spectral line analysis of galaxies at a relatively high z (Contini 2014a and references therein.)

In this paper we explore the origin of the observed Ly α and other lines in the UV from galaxies at $z < 3.7$ by detailed modelling of the spectra. Our aim is to find out not only the gas physical conditions and element abundances throughout the emitting

Table 1. The symbols in Fig. 1

	V_s km s $^{-1}$	n_0 cm $^{-3}$	$\log T_*$ [10 4 K]	$\log D$ [cm]	symbols	
AGN	100	100	-	17	black dotted	
	100	100	-	19	black dash-dotted	
	200	200	-	18	blue dotted	
	200	200	-	19	blue dash-dot	
	100	300	-	17	magenta dotted	
	100	300	-	19	magenta dash-dot	
	300	300	-	17	green dotted	
	300	300	-	19	green dash-dot	
	500	300	-	18	red dotted	
	500	300	-	19	red dash-dot	
	SB	100	100	4.0	19	red solid
		100	100	4.7	19	red dash-dot
		100	100	5.0	19	red dash
		200	200	4.0	19	blue solid
200		200	4.7	19	blue dash-dot	
200		200	5.0	19	blue dash	
300		300	4.0	19	magenta solid	
300		300	4.7	19	magenta dash-dot	
300		300	5.0	19	magenta dash	
500		300	4.0	19	black solid	
500		300	4.7	19	black dash-dot	
500		300	5.0	19	black dash	

clouds, but to determine the nature of the radiation source, such as a AGN, a SB or only shocks. The objects were chosen among those showing a) UV - optical - near-IR lines (Humphrey et al, Dawson et al, Stern et al, Erb et al and Fosbury et al), b) only UV lines (Vernet et al, Dey et al and Norman et al) and c) those showing Ly α in the UV and a few optical lines (Finkelstein et al). We also present UV line predictions for a sample of galaxies (Ly et al 2014) in the $0.0686 \leq z \leq 0.8829$ range, where the physical conditions of the emitting gas are constrained by the observed optical lines, in particular [OIII]4363. The total sample which includes galaxies in an all-sky radio survey, hard X-ray emitting sources, a type 2 QSR identified as a X-ray source, a type 2 AGN at high z (3.7), a very large spacially extended Ly α emitting nebula, objects in a multi-band imaging survey for Lyman break galaxies, in a slitless spectroscopic survey for LAEs, etc. is rather heterogeneous. However, the observed spectra from high z objects accounting for the Ly α line and for enough lines constraining the models, are few, so we gathered them from different classes of objects.

We calculate for each galaxy the gas density, temperature, shock velocity, etc., as well as the element abundances and the photoionizing source. The presence of an AGN or/and of a SB, collision heating and ionization of the ISM gas by shocks, the element abundances and dust survival throughout the clouds are important issues for middle and high redshifts galaxies which are tracers of star formation and evolution. The calculation models are briefly described in Sect. 2. Modelling results of the galaxy spectra are presented in Sect. 3. Results and concluding remarks are discussed in Sect. 4.

2. The calculation code

The line and continuum spectra emitted by gas and dust are calculated by the code `SUMA`¹. The code simulates the physical conditions in an emitting gaseous cloud under the coupled effect of photoionization from an external radiation source and shocks. The line and continuum emission from the gas are calculated

consistently with dust-reprocessed radiation in a plane-parallel geometry.

2.1. Input parameters

To calculate line and continuum fluxes emitted from a gas nebula, the temperature, density and element abundances should be known. In a shock dominated hydrodynamical regime the density profile throughout the nebula is shaped by the shock, while radiative and collisional heating and ionization of the gas are due to radiation from the external source (AGN, SB) and by the shock, respectively. The input parameters which characterise the shock are roughly suggested by the data, e.g. the shock velocity V_s by the FWHM of line profile and the pre-shock density n_0 by the characteristic line ratios and by the pre-shock magnetic field B_0 . We adopt $B_0 = 10^{-4}$ G, which is suitable to the NLR of AGN (Beck 2011).

The ionizing radiation from an external source is characterized by its spectrum and by the flux intensity. The flux is calculated at 440 energies, from a few eV to keV. If the photoionization source is an active nucleus, the input parameter that refers to the radiation field is the power-law flux from the active center F in number of photons cm $^{-2}$ s $^{-1}$ eV $^{-1}$ at the Lyman limit with spectral indices $\alpha_{UV} = -1.5$ and $\alpha_X = -0.7$. It was found by modelling the spectra of many different AGNs that these indices were the most suitable, in general. (see, e.g. Contini & Aldrovandi 1983, Aldrovandi & Contini 1984, Rodríguez-Ardila et al 2005, and references therein). In particular, for all the models presented in the following, we use $\alpha_{UV} = -1.5$, recalling that the shocked zone also contributes to the emission-line intensities, so that our results are less dependent on the shape of the ionizing radiation. The power-law in the X-ray domain was found flatter by the observations of local galaxies (e.g. Crenshaw et al 2002, Turner et al 2001). F is combined with the ionization parameter U by: $U = (F/(n c (\alpha_{UV} - 1))) ((E_H)^{-\alpha_{UV}+1} - (E_C)^{-\alpha_{UV}+1})$ (Contini & Aldrovandi, 1983), where E_H is H ionization potential and E_C is the high energy cutoff, n the density, α_{UV} the spectral index, and c the speed of light. If stars with a colour temperature T_* are the photoionization source, the number of ionizing photons cm $^{-2}$ s $^{-1}$ produced by the hot source is $N = \int_{\nu_0}^{\infty} B_\nu / h\nu d\nu$, where $\nu_0 = 3.29 \cdot 10^{15}$ Hz and B_ν is the Planck function. The flux from the star is combined with U and n by $N (r/R)^2 = U n c$, where r is the radius of the hot source, R is the radius of the nebula (in terms of the distance from the stars). Therefore, T_* and U compensate each other, but only in a qualitative way, because the black body radiation (which depends on T_*) determines the frequency distribution of the primary flux, while U represents the number of photons per number of electrons reaching the nebula. The choice of T_* and U is made by the fit of the line ratios.

In addition to the radiation from the primary source, the effect of the diffuse radiation created by the hot gas is also calculated, using 240 energies for the spectrum. The geometrical thickness of the emitting nebula D determines whether the model is radiation-bounded or matter-bounded. The dust-to-gas ratio (d/g) and the abundances of He, C, N, O, Ne, Mg, Si, S, A, Fe relative to H, are also accounted for. We adopt an initial grain radius $a_{gr} = 1 \mu\text{m}$.

2.2. Calculation process

The code accounts for the direction of the cloud motion relative to the external photoionizing source. A parameter switches between inflow (the radiation flux from the source reaches the

¹ <http://wise-obs.tau.ac.il/~marcel/suma/index.htm>

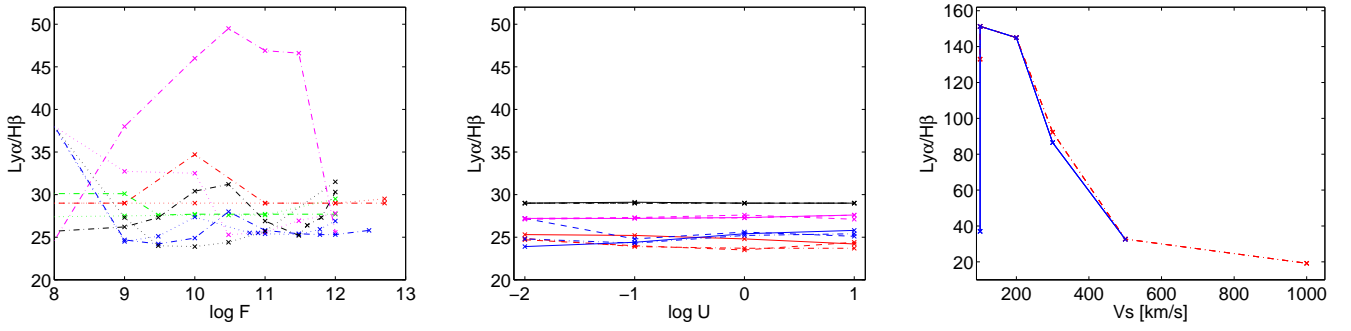


Fig. 1. Left: the Ly α / H β ratio calculated by the grid of models for the NLR of AGN (symbols are given in Table 1); centre : for SB (symbols in Table 1) right : for shock dominated spectra (red line : $D=10^{17}$ cm; blue line : $D=10^{19}$ cm)

Table 2. Modelling the spectra observed by Humphrey et al (2008)

	0211-122 ¹	FWHM ²	MH1	MH2	MH3	av	0406-244 ¹	MH4	MH5	av
z	2.340						2.440			
SFR(M_{\odot} yr ⁻¹)	24.85						911.			
Ly α 1216	0.21 \pm 0.01	1000	9.7	13.3	9.9	10.0	7.0 \pm 0.4	25.6	21.2	25.5
NV 1240	0.35 \pm 0.03		1.	3.87	0.005	0.2	<0.2	0.005	10.9	0.25
SiIV+OIV 1403	0.074 \pm 0.008		0.33	3.33	0.01	0.15	0.3 \pm 0.1	0.04	10.0	0.27
NIV]1485	0.024 \pm 0.005		0.07	0.83	0.007	0.04	<0.1	0.02	2.17	0.069
CIV 1549+	0.65 \pm 0.02		1.	7.67	0.15	0.5	0.9 \pm 0.1	0.31	20.7	0.772
HeII 1640	0.36 \pm 0.01	600	0.83	0.67	0.4	0.42	1.2 \pm 0.1	1.44	5.27	1.53
OIII]1667	0.028 \pm 0.003		0.13	1.23	0.04	0.1	0.2 \pm 0.1	0.09	3.6	0.17
CIII] 1909	0.17 \pm 0.03		0.33	3.67	0.46	0.5	0.9 \pm 0.1	0.8	9.9	1.0
CII] 2326	-		0.2	1.57	0.1	0.17	0.6 \pm 0.1	0.46	3.85	0.54
[NeIV]2423	0.11 \pm 0.01		0.07	0.7	0.03	0.06	1.0 \pm 0.3	0.09	8.0	0.3
[NeV] 3426	<0.3		0.07	0.7	0.02	0.05	0.5 \pm 0.1	0.05	1.8	0.1
[OII]3728+	0.39 \pm 0.08	730	0.17	1.33	0.45	0.48	2.6 \pm 0.2	2.65	3.7	2.67
[NeIII]3869	0.31 \pm 0.08	390	0.13	0.67	0.34	0.36	1.0 \pm 0.1	1.13	2.0	1.15
[OIII]4363	<0.4		0.02	0.2	0.032	0.04	-	-	-	-
HeII 4686	<0.2		0.07	0.07	0.03	0.036	0.21 \pm 0.06	0.2	0.4	0.21
H β quiescent	<0.5		0.33	0.33	0.33	0.33	1. \pm 0.7 ⁴	1.	1.	1.
[OIII] 5007+ quiescent	2.81 \pm 0.1	< 500	0.4	2.67	4.3	4.2	12.6 \pm 0.1	13.	10.0	12.9
[OIII] 5007+ perturbed	1.61 \pm 0.06	1300	-	-	-	-	-	-	-	-
[OI]	<0.2		0.10	0.67	0.09	0.11	-	1.3	0.58	1.28
H α quiescent	0.77 \pm 0.15 ³	< 500	1	1	1	1.0	3.3	2.9	3.1	2.9
H α perturbed	0.23 \pm 0.08	-	-	-	-	-	-	-	-	-
[NII] 6585+	<0.2	-	0.43	1.33	0.58	0.6	-	-	-	-
[SII] 6725+	<0.2	-	0.013	0.13	0.05	0.055	-	-	-	-
V_s (km s ⁻¹)	<0.2	-	1000	500	300	-	-	100	700	-
n_0 (cm ⁻³)	-	-	400	300	300	-	-	100	300	-
F^5	-	-	-	-	20	-	-	1.3	-	-
D^6	-	-	1	1	0.01	-	-	1	0.028	-
C/H ⁷	-	-	3.3	3.3	3.3?	-	-	3.3	3.3	-
N/H ⁷	-	-	1	1	1	-	-	1.	1.	-
O/H ⁷	-	-	6.6	6.6	6.6	-	-	6.6	6.6	-
S/H ⁷	-	-	-	-	-	-	-	0.02	0.02	-
H β calc ⁸	-	-	0.1	0.037	1.1	-	-	0.05	0.006	-
w	-	-	0.014	0.58	0.40	-	-	0.833	0.167	-

¹ in 10^{-16} erg cm⁻² s⁻¹; ² in km s⁻¹; ³ flux of narrow H α is $6.4 \pm 0.5 \cdot 10^{-16}$ erg cm⁻² s⁻¹; ⁴ flux of H β is $3.3 \pm 0.2 \cdot 10^{-17}$; ⁵ in 10^{10} photons cm⁻² s⁻¹ eV⁻¹ at the Lyman limit; ⁶ in 10^{19} cm; ⁷ in 10^{-4} units; ⁸ in erg cm⁻² s⁻¹

shock front edge of the cloud) and outflow (the flux reaches the edge opposite to the shock front). The calculations start at the shock front where the gas is compressed and thermalized adiabatically, reaching the maximum temperature in the immediate post-shock region ($T \sim 1.5 \times 10^5 (V_s / 100 \text{ km s}^{-1})^2$). T decreases downstream by the cooling rate and the gas recombines. The downstream region is cut into a maximum of 300 plane-parallel slabs with different geometrical widths calculated automatically, in order to account for the temperature gradient (Contini 2009 and references therein). In each slab, compression (n/n_0) is calculated by the Rankine–Hugoniot equations for the conservation of mass, momentum and energy throughout the shock front (Cox

1972). Compression ranges between 4 (the adiabatic jump) and > 100 , depending on V_s and B_0 . The stronger the magnetic field, the lower the compression downstream, while a higher shock velocity corresponds to a higher compression. The cooling rate is calculated in each slab by free-free (bremsstrahlung), free-bound and line emission. Therefore, most emission lines must be calculated in each slab even if only a few ones are observed because they contribute to the temperature slope downstream.

In pure photoionization models, the density n is constant throughout the nebula. In models accounting for the shocks, both the electron temperature T_e and density n_e show a characteristic profile throughout each cloud. The density reaches its upper

Table 3. Modelling the spectra by Humphrey et al (2008)

flux ¹	0529-549	MH6	MH7	0828	MH8	MH9	av	1138-262	MH10	MH11	4C+23.56	MH12	MH13
z	2.575			2.572				2.156			2.479		
SFR(M _⊙ yr ⁻¹)	150			86.				56.			163.		
Ly α 1216	-	27.0	21.2	21.7	45.	32.5	33.8	-	29.	27.6	2.17	47.5	30.4
NV 1240	-	0.07	10.9	0.9	24.	0.02	2.6	-	0.024	0.017	0.31	0.03+	0.06+
SiIV+OIV 1403	-	0.09	10.	0.78	2.3	0.05	0.3	-	0.02	0.013	0.05	0.19	0.13
NIV]1485	-	0.02	2.17	0.18	1.3	0.02	0.16	-	0.002	0.002	0.06	0.08	0.02
CIV 1549+	-	0.2	20.7	4.5	30.3	0.2	3.5	-	0.054	0.01	0.51	1.63	0.33
HeII 1640	-	0.83	5.27	2.57	5.8	1.	1.5	-	0.6	0.011	0.43	3.7	1.32
OIII]1667	-	0.065	3.6	0.46	3.15	0.1	0.43	-	0.04	0.009	0.11	0.37	0.11
CIII] 1909	-	0.55	9.9	1.4	4.2	1.1	1.43	-	0.46	0.1	0.28	0.7	1.
CII] 2326	-	0.56	3.85	0.48	3.4	0.9	1.17	-	0.35	0.1	0.22	0.19	0.85
[NeIV]2423	-	0.04	8.	1.2	2.	0.05	0.26	-	0.02	0.0027	0.37	0.26	0.06
[NeV] 3426	<2.1	0.018	1.8	0.76	8.85	0.012	0.98	-	0.01	0.0028	0.74	0.2	0.
[OII]3728+	3.2	3.3	3.7	1.75	2.1	3.7	3.5	1.44	1.35	1.2	2.57	2.7	3.4
[NeIII]3869	<2.1	1.0	2.	-	1.6	1.48	1.5	0.82	0.68	0.29	0.74	1.36	1.5
[OIII] 4363	<1	0.04.	0.63	-	-	-	-	-	-	-	-	-	-
HeII 4686	<1	0.12	0.4	0.29	0.44	0.15	0.18	<0.88	0.09	0.002	<0.86	0.53	0.2
H β	1.	1.	1	1	1	1	1	1	1	1	1	1	1
[OIII] 5007+	10.7	9.0	10	9.53	8.	11.8	11.4	6.	6.3	6.16	13.05	12.5	13.5
[OI] 6300+	0.58	1.1	-	-	-	-	-	<0.59	0.5	0.002	<0.28	0.7	1
H α	5.2	3.0	3.1	3	3	3	3	3	3	3	3	3	3
[NII] 6585+	2.6	2.76	0.	-	-	-	-	2.35	1.9	0.8	0.8	1.0	1.86
[SII] 6725	1.58	0.6	0.	-	-	-	-	0.85	0.63	0.1	0.86	0.8	0.7
V _s (km s ⁻¹)	-	180	700	-	700	1200	-	-	300	300	-	200	200
n ₀ (cm ⁻³)	-	100	300	-	400	400	-	-	300	300	-	300	300
T _* ²	-	-	-	-	-	-	-	-	-	4	-	25.	-
U	-	-	-	-	-	-	-	-	-	0.8	-	0.16	-
F ³	-	1.0	-	-	-	6	-	-	8	-	-	-	4
D ⁴	-	1	0.028	-	0.019	0.3	-	-	0.01	0.01	-	1.	0.01
C/H ⁵	-	3.3	3.3	-	3.3	3.3	-	-	3.3	3.3	-	0.8	0.8
N/H ⁵	-	1	1	-	1	1	-	-	1.	1	-	0.5	0.5
O/H ⁵	-	6.6	6.6	-	6.6	6.6	-	-	6.6	6.6	-	6.6	6.6
S/H ⁵	-	-	-	-	-	-	-	-	0.3	0.3	-	0.3	0.3
H β calc ⁶	-	0.06	0.0058	-	0.0089	0.29	-	-	0.62	1.6	-	0.59	0.14
w	-	-	-	-	0.8	0.2	-	-	-	-	-	-	-

¹ in 10⁻¹⁶ erg cm⁻² s⁻¹; ² in 10⁴ K; ³ in 10¹⁰ photons cm⁻² s⁻¹ eV⁻¹ at the Lyman limit; ⁴ in 10¹⁹ cm; ⁵ in 10⁻⁴ units; ⁶ in erg cm⁻² s⁻¹.

limit at a certain distance from shock-front and remains nearly constant, while n_e decreases following recombination.

The primary and secondary radiation spectra, calculated by radiation transfer, change throughout the downstream slabs, each of them contributing to the optical depth. In each slab of gas the fractional abundance of the ions of each chemical element is obtained by solving the ionization equations which account for photoionization (by the primary and diffuse secondary radiations and collisional ionization) and for recombination (radiative, dielectronic), as well as for charge transfer effects, etc. The ionization equations are coupled to the energy equation when collision processes dominate (Cox 1972) and to the thermal balance if radiative processes dominate (Williams 1967). The latter balances the heating of the gas due to the primary and diffuse radiations reaching the slab with the cooling due to line emission, dust collisional ionization and thermal bremsstrahlung. The line intensity contributions from all the slabs are integrated throughout the cloud. In particular, the absolute line fluxes referring to the ionization level i of element K are calculated by the term $n_K(i)$ which represents the density of the ion $X(i)$. We consider that $n_K(i) = X(i)[K/H]n_H$, where $X(i)$ is the fractional abundance of the ion i calculated by the ionization equations, $[K/H]$ is the relative abundance of the element K to H and n_H is the density of H (by number cm⁻³). In models including shock, n_H is calculated by the compression equation in each slab downstream. So the element abundances relative to H appear as input parameters. To obtain the N/H relative abundance for each galaxy, we consider the charge exchange reaction $N^+ + H \rightleftharpoons N + H^+$ (Steigman et al. 1971). Charge exchange reactions occur between ions with

similar ionization potential ($I(H^+) = 13.54$ eV, $I(N^+) = 14.49$ eV and $I(O^+) = 13.56$ eV). It was found that N ionization equilibrium in the ISM is strongly affected by charge exchange. This process as well as $O^+ + H \rightleftharpoons O + H^+$ (Field & Steigman 1971) are included in the SUMA code. The N^+/N ion fractional abundance follows the behaviour of O^+/O so, comparing the $[NII]/H\beta$ and the $[OII]/H\beta$ line ratios with the data, the N/H relative abundances can be easily determined (see Contini et al. 2012).

Dust grains are coupled to the gas across the shock front by the magnetic field. They are heated radiatively by photoionization and collisionally by the gas. up to the evaporation temperature ($T_{dust} \geq 1500$ K). The distribution of the grain radii downstream is determined by sputtering (Dwek 1981), which depends on the shock velocity and on the gas density. Throughout shock fronts and downstream, the grains might be completely destroyed by sputtering. The dust-to gas ratio d/g affects the mutual heating and cooling of gas and dust.

The calculations proceed until the gas cools down to a temperature below 10³ K (the model is radiation bounded) or the calculations are interrupted when all the lines reproduce the observed line ratios (the model is matter bounded). In case that photoionization and shocks act on opposite edges, i.e. when the cloud propagates outwards from the radiation source, the calculations require some iterations, until the results converge. In this case the cloud geometrical thickness plays an important role. Actually, if the cloud is very thin, the cool gas region may disappear leading to low or negligible low ionization level lines.

Summarizing, the code starts in the first gas slab adopting the input parameters given by the model. Then, it calculates the

density, the fractional abundances of the ions from each level for each element, free-free, free-bound and line emission fluxes. It calculates T_e by thermal balancing or the enthalpy equation, and the optical depth of the slab in order to obtain the primary and secondary fluxes by radiation transfer for the next slab. Finally, the parameters calculated in slab i are adopted as initial conditions for slab $i+1$. Integrating the line intensities from each slab, the absolute fluxes of the lines and of bremsstrahlung are obtained at the nebula. The line ratios to a certain line (generally H β for the optical-UV spectrum) are then calculated and compared with the observed data, in order to avoid problems of distances, absorption, etc. The number of the lines calculated by the code (more than 300) does not depend on the number of the observed lines nor on the number of input parameters, but on the elements composing the gas.

2.3. Selection of the models. The grids

The physical parameters are combined throughout the calculation of forbidden and permitted lines emitted from a shocked nebula. The ranges of the physical conditions in the gas are deduced, as a first guess, from the observed line ratios because they are more constraining than the continuum SED. We make use of the grids presented by Contini & Viegas (2001a,b) for AGN (GRID1) and SB (GRID2), respectively for a first estimate of the gas physical conditions. The grids were calculated by a gradual increase of the input parameters adapted from the observed issues. Grid results give a rough approximation to the observed spectra. Diagnostic diagrams for Ly α /H β calculated by the code SUMA for ejected clouds (Fig. 1) show that radiation dominated models (+shocks) lead to Ly α /H β between 20 and 30, with some higher values (up to 50) for low velocity, high density extended clouds. For shock dominated clouds Ly α /H β ranges between ~ 150 and ~ 15 .

The parameters are then refined by the detailed modelling of the spectrum. Specific grids of models are calculated for each galaxy modifying the parameters on small scales in order to reproduce as close as possible all the observed line ratios in each spectrum. We generally consider that the observed spectrum is "satisfactorily" fitted by a model when the strongest lines are reproduced by the calculation within 20% and the weak ones within 50%. "Satisfactorily" means that the approximation can be accepted 1) in the context of limits set by the author community, 2) considering the ensemble of all the line fit, 3) within the limits of the observational error, 4) if it can be improved only adopting unsuitable gas conditions, and 5) because, nevertheless, adding some information.

The final gap between observed and calculated line ratios is due to the observational errors both random and systematic, as well as to the uncertainties of the atomic parameters adopted by the code, such as recombination coefficients, collision strengths etc., which are continuously updated, and to the choice of the model itself.

The observed spectra provide averages throughout the whole galaxy, particularly at high redshifts. When the observed line ensemble is not satisfactorily reproduced by one model, the contribution of other regions within the galaxy at different physical conditions must be accounted for, leading to pluri-cloud models. The different results are summed up by relative weights (see, e.g. Rodriguez-Ardila et al. 2005) when they compensate each other (e.g. in Table 2). When they show similar results they are left as alternative proposals (e.g. Table 3).

The models selected by the fit of the line spectrum are cross-checked by fitting the continuum SED. In the UV range the

bremsstrahlung from the nebula is blended with black body emission from the star population background. The maximum frequency of the bremsstrahlung peak in the UV - X-ray domain depends on the shock velocity. In the IR range dust reprocessed radiation is generally seen (Contini, Viegas & Prieto 2004). In the radio range synchrotron radiation by the Fermi mechanism at the shock front is easily recognized by the slope of the SED.

The set of the input parameters which leads to the best fit of the observed line ratios determines the physical and chemical properties of the emitting gas. They are considered as the "results" of modelling.

3. Modelling single galaxy spectra

3.1. Spectra of the radio galaxies at $z \sim 2.5$ from the Humphrey et al (2008) survey

The long-slit NIR spectra obtained by the Infrared Spectrometer And Array Camera (ISAAC) instrument at VLT and completed with optical lines (by Keck and Subaru) contain a collection of lines in the wavelength range 1200-7000 Å. The observed Ly α /H β line ratios bridge between UV and optical data. Humphrey et al, modelling the spectra by pure radiation and pure shock models, concluded that the galaxies are most probably AGN in different physical conditions, with roughly solar abundances. We have selected dereddened (H α /H β ~ 3) spectra of galaxies containing the H β flux in order to compare the Ly α /H β line ratios (calculated at the nebula) with the observation data. We wish to investigate whether an SB contributes to some of the observed line ratios.

We consider all the line ratios in each spectrum (Tables 2 and 3), trying to reproduce them by models which account for the coupled effect of photoionization and shocks. The models are described in the bottom of the tables. Models corresponding to $F=0$ are shock dominated, i.e. the photoionising flux from the source outside the emitting nebula is hidden or absent. Similar shock dominated models are used to model supernova remnant spectra. The FWHM of the line profiles gives a hint about the shock velocity. Different FWHM of the lines in the UV and in the optical range indicate that the spectra emitted from different clouds within the galaxy should be considered. So pluri-cloud models are adopted. The weighted sum of the line ratios calculated by different theoretical models for each spectrum (e.g. col. 7 and 11 in Table 2) is compared with the observed line ratios. The weights adopted to sum the models are reported in the bottom row of the table.

In Table 2 we show the modelling of galaxies 0211-122 and 0406-244. The line fluxes are referred to H α = 1 for 0211-122 and to H β = 1 for 0406-244, following the Humphrey et al. notation. The H β flux is given as an upper limit for 0211-122. Considering that the calculated H α /H β line ratio is ~ 3 and the lines are referred to H α = 1, H β results ~ 0.33 , which is within the upper limit (0.5). Moreover, the spectrum is rich in lines from different elements in different ionization levels which can constrain the models. We focus on the [OII]3727+/[OIII]5007+ and CIV1549+/CIII]1909+/CII]2326+ line ratios (The + indicates that the doublet is summed) We could not find any model showing Ly α /H α as low as 0.2. By a shock dominated model with $V_s = 2000$ km s $^{-1}$ and $n_0 = 1300$ cm $^{-3}$ it is possible to obtain Ly α /H β = 7 (as for the 0406-244 galaxy) and even less. But in this case HeII 1640/H β = 9 and all the other line ratios = 0 destroy the good fit obtained by the radiation dominated model. High FWHM are adapted to the AGN broad line-emission region (BLR) (≥ 1000 km s $^{-1}$) rather than to the narrow line-emission

Table 4. Modelling UV spectra by Dawson et al (2003), Stern et al (2002) and Erb et al (2010)

	HDF ¹	FWHM ²	MDS	CX0 ³	FWHM ²	MSS	MSR	BX418 ⁴	FWHM	ME1-0	ME2-0	ME3	MESB
z	2.011			3.288				2.3					
SFR ($M_{\odot} \text{ yr}^{-1}$)	4.73			18.75				17.5					
OVI 1035	-	-	44.4	1.5:	2640	12.8	0.25	-	-	-	-	-	-
OV 1215	-	-	2.4	-	-	-	-	-	-	-	-	-	-
Ly α 1216	1.68	1270	1.5	18.9	1520	29.9	35.	11.27	840	35.	34.5	29.6	26.6
NV 1240	2.3	2100	2.2	0.6:	1820	0.65	0.16	-	-	-	-	-	-
SiIV+OIV 1403	-	-	-	0.4	1320	0.3+0.86	0.22	-	-	-	-	-	-
CIV 1549+	2.47	1300	2.2	3.5	1350	3.5	3.4	-	-	-	-	-	-
HeII 1640	0.45	1400	1.0	1.7	940	2.	3.0	0.31	612	0.3	0.31	0.89	0.003
[OII]1667	-	-	-	0.9	1290	0.3	0.4	0.23	235	0.033	0.06	0.14	0.02
CIII] 1909	0.19	900	0.3	2.1	1090	2.	1.9	0.54	225	0.16	0.27	0.88	0.2
NeIV] 2424	0.3	1470	0.20	-	-	-	-	-	-	-	-	-	-
[OII] 3727	-	-	-	-	-	-	-	<0.73	-225	0.045	0.09	0.65	0.66
H β 4861	-	-	0.1	1.2	170	1	1	1	<102	1	1	1	1
[OIII] 5007+	-	-	0.7	18.1	300-430	2.7	17.1	8.5	140	0.2	0.49	8.	8.88
[NII] 6584+6548	0.96	380	0.02	-	-	-	2.74	<0.12	-	0.28	0.48	0.2	0.22
H α n	0.7	240	-	-	-	-	3.	3.08	155	3.	2.9	3.3	3.
H α b	2.3	2500	0.278	-	-	2.7	-	-	-	-	-	-	-
V_s (km s^{-1})	-	-	1300	-	-	1500	200	-	-	840	600	260	260
n_0 (cm^{-3})	-	-	300	-	-	110	350	-	-	3000	3000	200	200
F^5	-	-	0	-	-	-	100	-	-	50	50	30	-
T_*^6	-	-	2.5	-	-	-	-	-	-	-	-	-	6.
U	-	-	8	-	-	-	-	-	-	-	-	-	0.7
D (10^{16}cm)	-	-	9.0	-	-	41.5	100	-	-	3.6	2.	400	400
C/H ⁷	-	-	2.6	-	-	3.3	3.3	-	-	3.3	3.3	3.3	3.3
N/H ⁷	-	-	1.	-	-	0.4	0.1	-	-	0.3	1.0	0.3	0.3
O/H ⁷	-	-	6.6	-	-	3.6	6.6	-	-	6.6	6.6	6.6	6.6
H β calc ⁸	-	-	0.0085	--	-	0.035	1.77	-	-	10.8	4.5	1.65	0.91

¹ HDFx28 (Dawson et al 2003) in $10^{-17} \text{ erg cm}^{-2} \text{ s}^{-1}$; ² in km s^{-1} ; ³ CXO J084837.9+445352 (Stern et al 2002) in $10^{-17} \text{ erg cm}^{-2} \text{ s}^{-1}$; ⁴ BX418 (Erb et al 2010) in $2.6 \cdot 10^{-17} \text{ erg cm}^{-2} \text{ s}^{-1}$; ⁵ in $10^{10} \text{ photons cm}^{-2} \text{ s}^{-1} \text{ eV}^{-1}$ at the Lyman limit; ⁶ in 10^4 K ⁷ in 10^{-4} ; ⁸ in $\text{erg cm}^{-2} \text{ s}^{-1}$;

region (NLR). Forbidden lines such as [OII] 3727 are generally collisionally deexcited in the BLR due to the high density. Low Ly α /H α perhaps indicates strong absorption by dust in the nebula. The results presented in Table 2 show that the lines come from different clouds within the galaxy. The highest ionization level lines are stronger where collisional ionization dominates. HeII 1640, which is a recombination line, increases with both the temperature of the gas and the photoionization flux.

For 0211-122 we group the shock velocities into two prototypes. $V_s \sim 1000 \text{ km s}^{-1}$ representing high velocity shocks fits the UV lines, while $V_s \leq 500 \text{ km s}^{-1}$ reproduces the lines in the optical range. The results of selected models appear in cols. 4, 5 and 6. The weighted sum of the line fluxes appears in col. 7 of Table 2, Models MH1 and MH2 which refer to $V_s = 1000 \text{ km s}^{-1}$ and 500 km s^{-1} , respectively, are shock dominated (SD, $F=0$), while model MH3 with $V_s = 300 \text{ km s}^{-1}$ is radiation dominated (RD) +shock. Model MH2 is included because, overpredicting the CIV and [OII] 3727 lines, improves the approximation of the averaged spectrum. O/H is solar and N/H seems lower than solar by a factor of ~ 3 . We refer to the solar abundances by Allen (1976). They are discussed by Contini (2014a). The average model overpredicts the OIV]/H α , NIV]/H α and CIII]/H α multiplet ratios to H α because the calculations account for the sum of all the multiplet terms. We do not know which terms are included in the observation data. Different geometrical thickness of the clouds D indicate fragmentation by shock in a turbulent regime. The 0406-244 spectrum is satisfactorily reproduced by the weighted sum (av in column 11) of models MH4, dominated by the AGN radiation, and MH5, dominated by the shock. The relative weights were calculated phenomenologically in order to obtain the best approximation to the spectrum, even if some line ratios (e.g. [NeV]) are less fitted. Also for this galaxy a SD model (MH5) corresponds to the highest V_s (700

km s^{-1}). More spectra of selected galaxies from the Humphrey et al sample are shown and modelled in Table 3.

The FWHM of the line profiles range between 600 and 900 km s^{-1} . They are not reported in the table for sake of space. In Table 3 we refer all the spectra to H β =1 in order to easily compare observed line ratios to model results from different galaxies. The spectrum presented for 0529-549 in Table 3 shows a few line ratios. Most are upper limits. Both [OIII] 5007+/H β line ratios calculated by high V_s and low V_s models reproduce satisfactorily the data. [NII]/H β and [SII]/H β depend strongly on the N/H and S/H relative abundances, respectively. So, an averaged model is not significant. The modelling of 0828 suggests that carbon should be depleted by a factor of ~ 5 from the gaseous phase, most probably trapped into grains throughout the nebula represented by model MH8. Neon cannot be included into dust grains because of its atomic structure, then we determine the relative weights of the averaged model av by fitting the [NeV]/H β line ratio. Model av (col. 8) shows that, in contrast to our previous hypothesis, C/H solar is suitable to the high velocity gas component of 0838. The observed lines of 1138-262 are few and the oxygen lines are well approximated by both the AGN and SB dominated models, therefore the relative weights in an eventual average spectrum are less constrained. Galaxy 4C+23.56 spectrum shows a non negligible [NeV], while model MH13 yields [NeV]=0, therefore the SB dominated model MH12 is more appropriated.

The main conclusions by Humphrey et al. are in agreement with our modelling. Namely, 1) AGN photoionization with U varying between the objects is generally indicated. However, we find an SB contribution to 1138-262 and 4C+23.56 spectra; 2) single-slab photoionization models are unable to reproduce satisfactorily the high and low ionization lines simultaneously; 3) shocks alone do not provide a valid explanation but must be added to a photoionization source; 4) N/H is nearly solar for all

Table 5. Modelling the spectra from the observations of Vernet et al (2001)

Flux ¹	4C+03.24	MV1	0943-242	MV2	MV3	0731+438	MV4	MV5	av	4C-00.64	MV6
z	3.560		2.922			2.429				2.360	
SFR ²	192.3		100.6			128.6				73.27	
OVI	-	-	5.6	4.3	9.5	-	-	-	-	-	-
OV	4.8 \pm 0.8	7.3	-	-	-	-	+	-	-	-	-
Ly α	254.4 \pm 7.3	237.	213.8 \pm 1.8	240.	263.	428.1 \pm 2.2	426.	455.	445.	261.6 \pm 3.4	233.
NV	4.8 \pm 0.8	5.2	11.2 \pm 0.6	4.4	14.2	7.1 \pm 0.6	8.0	7.7	7.8	12.4 \pm 1.2	15.3
CII	4.6 \pm 1.3	1.6	2.4	0.7	2.2	2.2	1.4	0.7	0.94	1.1	1.4
OIV+SiIV	6.1 \pm 2.5	5.0	8.9	9.1	16.	9.7	13.0	3.9	7.0	10.4	14.
NIV]	-	-	2.4	4.	6.8	1.8 \pm 0.3	3.0	2.5	2.67	-	-
SiII	-	-	1.2	-	-	0.9	-	-	-	-	-
CIV	12.5 \pm 2.2	10.5	46.5 \pm 1.1	55.2	40.	46.5 \pm 1.0	17.	47.3	36.9	29.1 \pm 2	30.07
[NeV]	-	-	-	0.4	0.62	-	-	-	-	-	-
HeII	5.2 \pm 1.3	6.0	47.1 \pm 1.3	71.8	22.8	30.4 \pm 0.5	23.	19.6	20.8	21.5 \pm 0.5	11.2
OIII]	-	-	7.6	4.	6.	6.4	1.7	2.4	2.16	3.6	4.
NIII]	-	-	1.4	2.	2.9	-	0.5	1.2	0.96	-	-
SiII	-	-	1.7	-	-	1.4	-	-	-	-	-
SiIII]	-	-	5.4	1.4	1.6	2.7	0.1	1.1	0.8	-	-
CIII]	-	-	29.3 \pm 3.1	24.	14.	21.2 \pm 0.5	1.4	24.8	16.9	9.6 \pm 0.7	11.7
H α	30.5	-	25.66	-	-	51.36	-	-	-	31.4	-
V _s ³	-	130	-	100	130	-	140	140	-	-	120
n ₀ ⁴	-	60	-	100	150	-	150	130	-	-	60
F ⁵	-	-	-	2.5	-	-	-	6.	-	-	-
T _* ⁶	-	4.55	-	-	6	-	5	-	-	-	4.5
U	-	0.7	-	-	0.15	-	0.9	-	-	-	0.7
D ⁷	-	0.013	-	0.01	0.0008	-	0.001	0.1	-	-	0.01
C/H ⁸	-	3.3	-	3.3	3.3	-	3.3	3.3	-	-	3.3
N/H ⁸	-	1.	-	1.	1.	-	1.	1.	-	-	1.
O/H ⁸	-	6.6	-	6.6	6.6	-	6.6	6.6	-	-	6.6
H β ⁹	-	0.009	-	0.012	0.009	-	0.014	0.13	-	-	2.6e-4
w	-	-	-	-	-	-	0.97	0.03	-	-	-

¹ in 10^{-17} erg cm⁻² s⁻¹; ² in M_⊙ yr⁻¹; ³ in km s⁻¹; ⁴ in cm⁻³; ⁵ in 10^{10} photons cm⁻² s⁻¹ eV⁻¹ at the Lyman limit; ⁶ in 10^4 K; ⁷ in 10^{17} cm; ⁸ in 10^{-4} units; ⁹ calculated in erg cm⁻² s⁻¹

Table 6. Modelling the spectrum of the SST24 J1434110+331733 nebula (Dey et al 2005), CDF-S202 (Norman et al 2002) and Lynx arc (Fosbury et al 2003)

flux	SST24 ¹	MDR	MDOS	MDSB	av	CDF-S202 ²	FWHM ³	MNR	MNS	Lynx ⁴	MF0	MFSB
z	2.656					3.7				3.36		
SFR (M _⊙ yr ⁻¹)	134.6					136.2				177.8		
Ly α 1216	28.9 \pm 0.15	-	-	-	-	-	-	-	-	-	-	-
Ly α 1216	4.05 \pm 0.01	-	-	-	-	-	-	-	-	-	-	-
Ly α 1216	3.10 \pm 0.01	3.03	3.3	4.9	3.39	16.4	<1130	28.	22.6	10.8	31.8	38.
NV 1240	<0.05	0.017	0.03	0.1	0.03	5.9	<1680	0.	8.75	\leq 0.09	0.3	0.001
SiIV 1397	-	-	-	-	-	-	-	-	-	\leq 0.09	0.09	-
NIV] 1483+	-	-	-	-	-	-	-	-	-	0.42	0.15	0.05
CIV 1549+	0.417 \pm 0.001	0.6	0.47	0.4	0.49	9.9	<1680	3.19	12.2	3.65	3.6	0.46
HeII 1640	0.4 \pm 0.004	0.82	0.39	0.3	0.45	2.8	<680	0.7	6.48	0.11	0.11	0.12
OIII] 1661+	-	-	-	-	-	-	-	-	-	0.56	0.48	0.09
NIII] 1750	-	-	-	-	-	-	-	-	-	0.18	0.1	0.12
SiIII] 1883+	-	-	-	-	-	-	-	-	-	0.15	0.14	0.06
CIII] 1909	0.05 \pm 0.01	0.0013	0.18	0.03	0.13	-	-	12.8	4.8	0.59	1.4	1.0
[OII] 3727+	-	-	-	-	-	-	-	-	-	\leq 0.25	0.17	0.57
[NeIII] 3869+	-	-	-	-	-	-	-	-	-	\leq 0.91	0.2	1.16
HeII 4686	-	-	-	-	-	-	-	-	-	\leq 0.22	0.01	0.02
H β	-	0.1	0.1	0.1	0.1	1	-	1	1	1	1.	1
[OIII] 5007+	-	-	-	-	-	-	-	-	-	10.1	0.7	9.
5084	0.52 \pm 0.004	-	-	-	-	-	-	-	-	-	-	-
H α 6563	0.371	0.3	0.3	0.3	0.3	1.97	-	3.	3.	-	3.7	3.1
V _s (km s ⁻¹)	-	1700	1700	300	-	-	-	1600	1600	-	320	100
n ₀ (cm ⁻³)	-	110	110	150	-	-	-	120	120	-	2000	300
F ⁵	-	100	-	-	-	-	-	1	-	-	-	-
T _* ⁶	-	-	-	2.5	-	-	-	-	-	-	-	1.1
U	-	-	-	8	-	-	-	-	-	-	-	0.3
D (10 ¹⁷ cm)	-	300	3.	5.	-	-	-	100	15	-	1	4900
C/H ⁷	-	3.3	3.3	3.3	-	-	-	3.3	3.3	-	3.3	3.3
N/H ⁷	-	1.	0.1	1.	-	-	-	1.	1.	-	0.2	1.0
O/H ⁷	-	6.6	6.6	6.6	-	-	-	6.6	6.6	-	6.6	3.6
H β calc ⁸	-	0.0336	0.024	5.68	-	-	-	200.	0.0085	-	0.15	8.7
w	-	0.137	0.822	0.041	-	-	-	-	-	-	-	-

¹ 10^{-16} erg cm⁻² s⁻¹ (Dey et al.); ² 10^{-16} erg cm⁻² s⁻¹; (Norman et al (2002)); ³ in km s⁻¹; ⁴ in 10^{-17} erg cm⁻² s⁻¹ eV⁻¹ at the Lyman limit; ⁵ in 10^{10} photons cm⁻² s⁻¹; ⁶ in 10^5 K; ⁷ in 10^{-4} units; ⁸ in erg cm⁻² s⁻¹

objects and does not vary as much as by a factor of 2-3; 5) The line FWHM and the ionization state are the result of interaction between the clouds in terms of shocks, when the radiation from the AGN or the SB is absent.

3.2. HDFX 28, a spiral galaxy at $z=2.011$ from the observations of Dawson et al. (2003)

In search for type 2 QSRs, HDFX 28 was identified as a face-on spiral galaxy at $z=2.011$. Initially, it was considered as an extended radio source powered by star formation (Richards 2000), but the hard X-ray source and the spectroscopy demonstrated that this galaxy contains an obscured type 2 AGN (Dawson et al and references therein). The galaxy was observed by ISOCAM and Chandra. Table 4 shows that a SB dominated model (MDS) roughly reproduces the data. Dawson et al spectrum contains too few narrow lines, [NII] 6548, 6548 and H α to provide a consistent modelling of the low V_s gas. On the basis of [NII] 6548+6584/H α , we can predict that, if the reddening is negligible and H α /H β = 3, [NII]/H β = 4.11, which indicates for a SB model $U \leq 0.1$, $T_* = 1-4 \cdot 10^4$ K, $V_s = 220$ km s $^{-1}$, $n_0 = 200$ cm $^{-3}$, $D = 10^{19}$ cm and solar abundances. For an AGN model, such line ratios can be obtained with N/H solar, $V_s = 100-250$ km s $^{-1}$ and $F \leq 10^9$ photons cm $^{-2}$ s $^{-1}$ eV $^{-1}$ at the Lyman limit, and for $V_s = 500$ km s $^{-1}$ and $F \leq 10^{10}$ photons cm $^{-2}$ s $^{-1}$ eV $^{-1}$ at the Lyman limit. Such [NII]/H β can be also obtained by a SD ($F=0$) model with $V_s = 300$ km s $^{-1}$. The preshock densities are 100-300 cm $^{-3}$ and the geometrical thickness of the emitting clouds are between 10^{17} and 10^{19} cm. In conclusion, the [NII]/H β line ratio alone cannot constrain the narrow line model.

In Fig. 2 we present the modelling of the continuum SED. The data are given by Dawson et al 2003, table 1). The continuum SED calculated by the code SUMA shows two curves for each model. One represents the bremsstrahlung from the gas and the second one, in the IR, represents reprocessed radiation from dust. The data in the radio - UV - soft-X-ray range are well fitted by the high V_s , SB dominated model MDS. Harder X-ray data in Fig. 2 could be reproduced by a model calculated by a shock velocity even higher than 1500 km s $^{-1}$, as suggested by the FWHM of some line profiles. The AGN and the SB dominated models calculated by $V_s = 220$ km s $^{-1}$, which were predicted on the basis of the [NII]/H β line ratio, reproduce the data in the optical range, in agreement with the H α narrow line FWHM. The modelling of the HDF galaxy continuum SED constrains the choice of the low velocity model, but it cannot select between an AGN or a SB.

3.3. Spectrum from CXO 52 by Stern et al. (2002) observations

CXO 52 was identified as an optical, colour selected, high redshift source (Stern et al 2002c) and by optical follow up of X-ray sources in the Lynx field (e.g. Stanford et al 1997). Stern et al (2002) report on observations of a type 2 quasar at $z=3.288$ that was identified as a hard X-ray source by Chandra X-ray observatory. The optical spectrum of CXO 52 was obtained by Keck I telescope. Line profile FWHM are broad (≥ 1000 km s $^{-1}$). A shock dominated model with $V_s = 1500$ km s $^{-1}$ and pre-shock density $n_0 = 110$ cm $^{-3}$, resembling those found in other galaxies at similar redshifts, fits most of the UV lines (MSS Table 4). The Ly α /H β is overpredicted by a factor of 1.6. OVI1035/H β is underpredicted and NV 1240/H β is well reproduced. The maximum temperature of the gas downstream, near the shock-front depends on the shock velocity (Sect. 2) therefore, MSS model

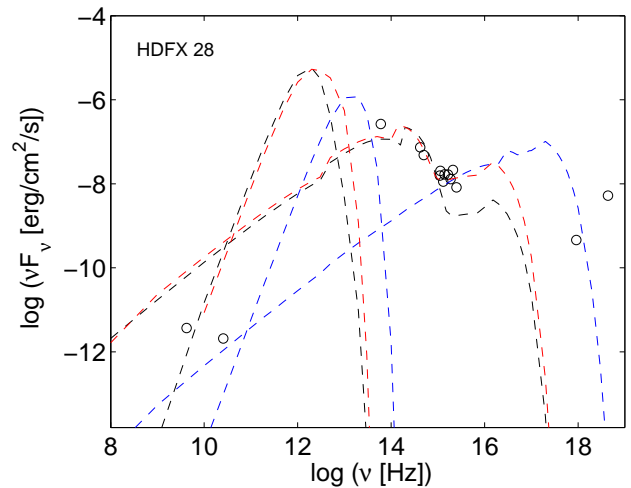


Fig. 2. Modelling the continuum SED observations Dawson et al. (2002, table 1 and references therein). Blue lines: the shock dominated model MDS model; black lines: the AGN radiation dominated model calculated by $V_s = 220$ km s $^{-1}$, $n_0 = 200$ cm $^{-3}$, $\log F = 9$, and solar abundances; red lines: the SB radiation dominated model calculated by $T_* = 3 \cdot 10^4$ K and $U = 0.1$.

fits NV/H β because NV is a high ionization level line. OVI which shows a FWHM = 2640 km s $^{-1}$ cannot be well reproduced by model MSS.

The H β and the forbidden lines [OIII]5007+ correspond to lower FWHM (170-430 km s $^{-1}$). The lines are emitted from clouds within the galaxy with different V_s . A radiation dominated model (MSR) with $V_s = 200$ km s $^{-1}$ and $n_0 = 350$ cm $^{-3}$ reproduces the UV lines (except OVI and NV) within a factor of 2 and explains the high [OIII]5007+4959/H β . The flux from the AGN corresponds to a Seyfert 2. The results of the two models are not summed up because they show very different gas conditions in (most probably) well separated regions throughout the galaxy.

To cross check the models we compare the bremsstrahlung calculated by models MSS and MSR with the data presented by Stern et al (in their table 1) in Fig. 3. The datum at 2-10 keV is well reproduced by model MSS, calculated by a high shock velocity. The bremsstrahlung maximum depends on the maximum temperature of the gas downstream. Dust grains can be completely destroyed by sputtering at high shock velocities (> 1000 km s $^{-1}$). The grains in the nebulae represented by models MDS and MSS are characterised by a relatively large initial radius ($a_{gr} = 1 \mu\text{m}$) in order to survive to strong sputtering throughout a high velocity shock-front. However, they can be completely destroyed by sputtering and evaporation, as happens for model MSS, depending on the cooling rate downstream. The relatively low V_s which characterises the gas conditions in model MSR yields grain survival. The bremsstrahlung calculated by model MSR, which corresponds to gas ionised and heated by the flux from the AGN (+shocks), roughly fits the data in the UV-optical and radio ranges. The reprocessed radiation by dust in the IR is constrained by only one datum which leads to $d/g = 10^{-4}$ by mass.

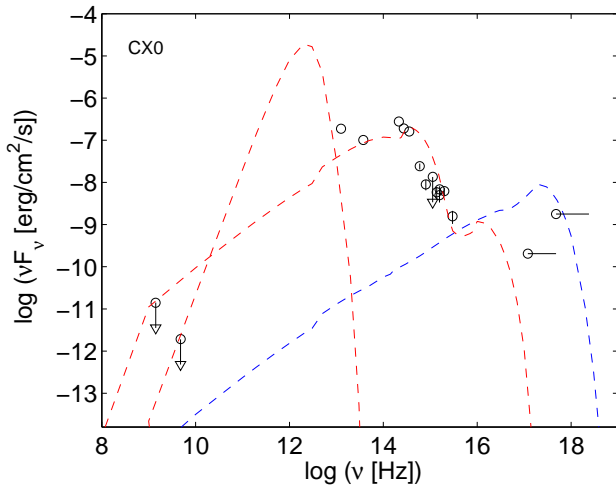


Fig. 3. Modelling the continuum SED observations Stern et al. (2002, table 1 and references therein). Blue lines: the shock dominated model MSS model; red lines : the radiation dominated model MSR;

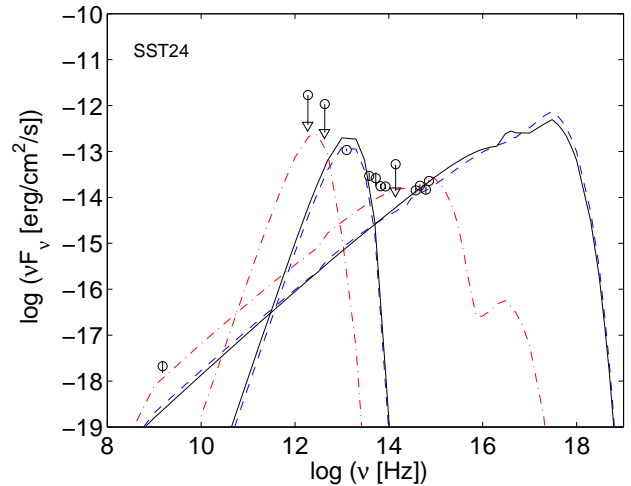


Fig. 4. The continuum SED modelling of Dey et al. data. Blue lines: the AGN model; red lines : the SB model; black lines: the shock dominated model and reradiation by dust at 1000 K

3.4. The spectrum observed from Q2343-BX418 by Erb et al (2010)

In column 9 of Table 4 we present the observed line ratios for BX418 galaxy at $z=2.3$, defined by Erb et al., as "one of the youngest and lowest stellar mass continuum-selected $z \sim 2$ galaxies".

The spectral lines show different FWHM for different wavelengths decreasing from $\sim 840 \text{ km s}^{-1}$ for Ly α to 640 km s^{-1} for HeII 1640, down to $\leq 260 \text{ km s}^{-1}$ for lines in the optical-near-UV range (Table 4, col 10). The observations show that different components contribute to different lines. Although permitted line fluxes (e.g. Ly α and HeII) depend strongly on the photoionizing radiation reaching the nebula, they also increase with the temperature of the emitting gas (see Sect. 3.8). Therefore, models accounting for shock+ photoionization are used. The models are presented in Table 4. We first investigate whether an AGN (hidden?) is present. The high Ly α and HeII 1640 FWHM suggest shock velocities of ~ 850 and $\sim 600 \text{ km s}^{-1}$, respectively. They are accompanied by a AGN flux characteristic of Seyfert 2 galaxies. The densities are high throughout the nebula to reduce the primary and secondary fluxes rapidly enough. The temperature drop will lead to very low line intensities in the optical range. Actually, broad optical lines were not observed. We could not obtain acceptable results with models corresponding to outflow of the gas, on the contrary, gas inflow towards the AGN is indicated (models ME1-0 and ME2-0). We reproduced the near UV and optical line ratios by models corresponding to the NLR conditions. Models ME3 and MESB roughly fit the [OII]/H β and [OIII]/H β line ratios. ME3 refers to an AGN, while MESB refers to a SB radiation source. Both shows outflow of gas from the galaxy and are similar to those found in other galaxies at those redshifts. We suggest that all the gas conditions represented by the models in Table 4 are present within BX418, contributing to the single lines in the spectrum. The models are not summed up, in order to show each contribution to each line. BX418 has been placed among metal-poor galaxies (Erb et al). However, the low metallicity (0.05 solar) was calculated by Erb et al by the strong-line metallicity diagnostic as well as by the direct methods. They found $12 + \log(\text{O}/\text{H}) = 7.9 \pm 0.2$, while the results

of detailed modelling yield solar $12 + \log(\text{O}/\text{H}) = 8.812$. The discrepancy between metallicities calculated by direct methods and modelling has been discussed by Contini (2014b).

3.5. Spectra by Vernet et al (2000) at $z \sim 2.5$ and the diagrams

Vernet et al (2001) present spectropolarimetry of powerful extragalactic radio sources at $z \sim 2.5$ by Keck II telescope, "when quasars were much more common than now". Although dust-reflected quasar light dominates the UV continuum, they did not exclude star formation. Vernet et al. comparing the data throughout the NV/HeII vs NV/CIV diagrams by Hamann & Ferland (1993) could not easily explain the observed NV/CIV and NV/HeII line ratios. In Sect. 4 we will discuss Vernet et al and other survey observations throughout the HeII/CIV vs Ly α /CIV diagrams, where the data are compared with model results calculated by SUMA. UV line ratios are generally referred to CIV which is one of the strongest lines. Moreover, we have found that the N/H relative abundances throughout galaxies are scattered by a factor of ~ 10 (Contini 2014a, fig. 5), therefore we suggest that NV lines are less adapted to diagnostic diagrams.

We present in Table 5 the results of shock+photoionization models for some of the Vernet et al spectra. 4C+40.36 and 4C+48.48 were excluded because the spectra are most probably blended by a foreground HII galaxy at $z=0.404$ and at $z=0.684$, respectively. The modelling results indicate that composite models referring to the SB+shocks, to the AGN+shocks should be adopted and that different physical conditions from different regions contribute to the spectra. All the models used to reproduce Vernet et al data in Table 5 show relatively low V_s and n_0 , which are reflected in low SFR. Vernet et al found a SFR range between $\sim 60 M_\odot \text{ yr}^{-1}$ to $\leq 2 M_\odot \text{ yr}^{-1}$. They claim that in 0731+438 the only object where reprocessed radiation from AGN does not dominate the continuum (for the other objects starlight contributes less than half of the UV continuum, see Vernet et al 2001, table 5) and assuming $E(B-V)=0.1$ and a stellar population age of 10^9 yr, Vernet et al calculate SFR between 30 and $120 M_\odot \text{ yr}^{-1}$. Our calculations give SFR $\sim 128 M_\odot \text{ yr}^{-1}$ for 0731+438, a minimum SFR ~ 24.4 for 4C+23.56a, etc. (see Table 5)

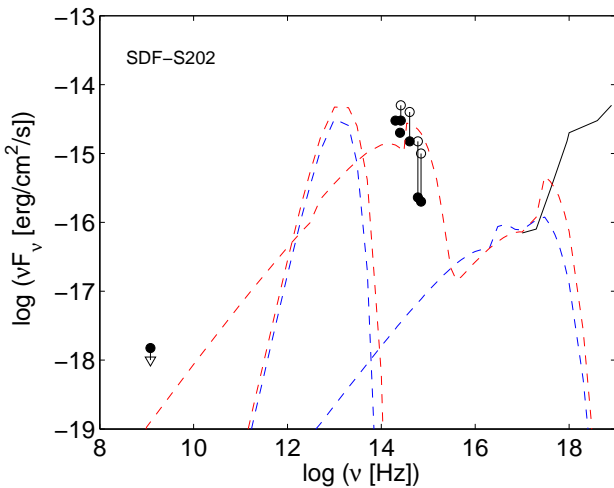


Fig. 5. The continuum SED modelling of SFD-S202. The data are adapted from Norman et al. (2002, fig. 6) Blue lines: the shock dominated model MNS; red lines : the AGN model MNR. black solid line : the X-ray data

3.6. Line and continuum observations of an extended nebula by Dey et al. (2005)

Massive ellipticals at high z (≥ 3) are surrounded by large (100-200 kpc) luminous ($> 10^{43}$ erg s^{-1}) Ly α nebulae and small embedded star forming objects. Investigating (> 100 kpc) halos and environments of luminous radio galaxies affected by AGNs and ejecta of similarly large Ly α nebulae, Dey et al (2005) reported on observations of a very large, spatially extended (160 kpc) Ly α emitting nebula at $z=2.656$. Spectroscopic observations of SST24 J1434110+331733 were obtained by the Low Resolution Imaging Spectrometer (LRIS) on the Keck I telescope.

The spectroscopic observations reveal very complex regions within the extended nebula, including several continuum sources. Dey et al suggest that many active galaxies are forming in that region which lead to three main contributions to the continuum spectrum. Galaxy A shows interstellar absorption lines and no Ly α emission; the spectrum of the second continuum source is quite red and shows weak CIV and CIII] emission at $z=2.656$. Star formation is suggested because the source is close to MIPS 24 μ m location. The third continuum source lies in the centre of the Ly α nebula associated to CIV and HeII. The velocity structure of the nebula deduced from the line profiles shows that the velocity varies uniformly across the central region. If due to gas kinematics, the variation can be due to infall, outflow, or rotation.

We refer to the line and continuum observations by Dey et al. The results of modelling are presented in Table 6. On the basis of the observed lines corresponding to broad profiles, we have run models with $V_s > 1000$ km s^{-1} . We find a large contributions to the line fluxes from high velocity ($V_s = 1700$ km s^{-1}) shock dominated gas (models MDOS) and photoionized by an AGN (model MDR). Moreover, the contribution from gas with $V_s = 300$ km s^{-1} and photoionised by a SB is evident (MDSB). The high velocities are at the limit of those observed in AGN NLR. The AGN flux is characteristic of Seyfert 2. The starburst temperature which leads to a satisfactory fit of the line ratios ($2.5 \cdot 10^5$ K) is as high as that found in galaxies showing activity (Contini 2014b). Also the ionization parameter is high. The gas throughout the SB shows "normal physical conditions" in

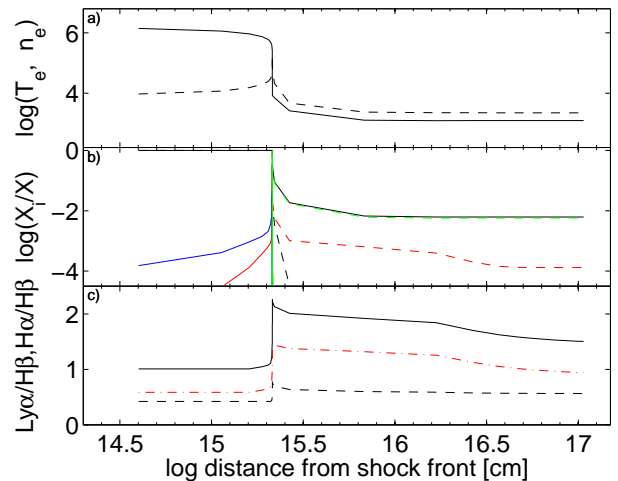


Fig. 6. The profiles of the physical quantities throughout the emitting nebula for the SD model MF0. The shock-front is on the left. Top : electron temperature (solid black), electron density (dashed black). Middle : H $^+$ /H (solid black), He $^{++}$ /He (dashed black), C $^{2+}$ /C (dashed red), C $^{3+}$ /C (solid red), N $^{4+}$ /N (solid blue), O $^+$ /O (dashed green), O $^{2+}$ /O (solid green). Bottom : log (Ly α /H β) (solid black), log(H α /H β) (dashed black) and log(Ly α /H α) (dot-dashed red).

the emitting nebulae of galaxies at such redshifts. However, to have a good fit of the NV 1240 line, we have adopted N/H lower than solar by a factor of ~ 10 in the shock dominated gas. This indicates that it is located in a different region of the galaxy. The weighted sum of the calculated spectra (av) appears in Table 6 col. 6. We suggest that the λ 5084 line refers to scandium ($^4F_{3/2} - ^4F_{9/2}$, White 1934, fig.14.7). Scandium can be present in SN ejecta (e.g. Bose et al. 2015).

Fig. 4 shows that the continuum SED calculated by the models selected by fitting the line ratios reproduce the observed continuum data presented by Dey et al. (2005, fig.2). Bremsstrahlung from gas heated by the strong shock shows a maximum at high frequency (Contini, Viegas, Prieto 2004). X-ray emission is predicted. The mass of the emitting gas ($6 \cdot 10^{12}$ M_\odot) was calculated by Dey et al. The mass of dust can be calculated by $d/g = 0.003$ by mass which results from the fit of the continuum SED in the IR.

3.7. A classic type 2 QSO at $z=3.7$: CDF-S202 observations by Norman et al (2002)

Norman et al observed the AGN detected at $z=3.7$ by the Chandra Deep Field-South 1 Ms exposure. It is a distant type 2 AGN with UV showing FWHM of ~ 1500 km s^{-1} . The optical spectrum was obtained with the multislit mode on the FORS1 on the ESO/VLT-ANTU. Detailed modelling (Table 6, cols. 9, 10) indicates that a shock dominated model (MNS) best fits the lines within a maximum discrepancy factor of 2.3 for HeII 1640 (Table 6 last column). This model calculated by $V_s = 1600$ km s^{-1} would provide OVI 1035/H β ~ 200 . Norman et al found a high metallicity, while we suggest N/H by a factor of 1.5 lower than solar and C/H about solar, considering the uncertainty of the line fluxes. Referring the line to CIV=10 instead of H β , as it is generally done for UV spectra, we would obtain an acceptable fit of all the lines. The radiation (AGN+shock) dominated model (MNR) calculated by the high V_s reproduces the line ra-

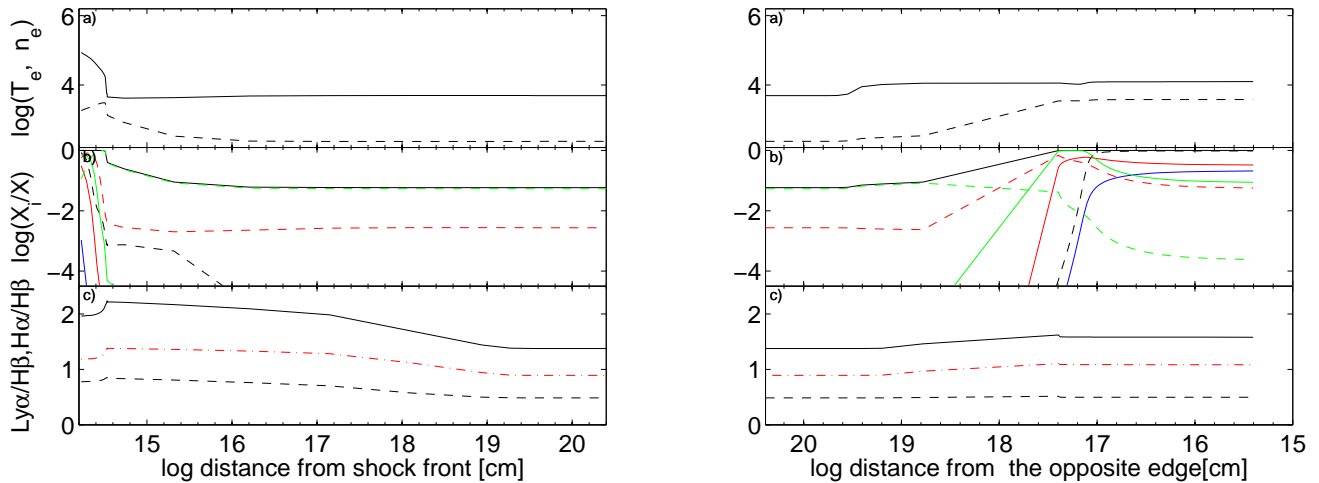


Fig. 7. Same as in Fig. 6 for model MFSB

tios roughly. In Fig. 5 we present the modelling of the continuum SED. The data were adapted from Norman et al. fig. 6. The continuum calculated by the radiation (+shock) dominated model MNR reproduces the data in the optical-UV better than the shock dominated model MNS, so the MNR model should be accounted for, but with a low relative weight.

3.8. Spectrum of the Lynx arc at $z=3.357$ by Fosbury et al (2003)

The Lynx arc ($z=3.357$) is characterised by a very red R-K colour and strong, narrow emission lines. Fosbury et al claim that analysis by HST WFPC2 imaging and Keck optical and IR spectroscopy indicate a HII galaxy magnified by a factor of 10 by a cluster environment including stars with $T_* \sim 10^6$ K, $U \sim 1$ and low metallicity (0.05 solar). In Table 6, col 11 the observed spectrum of the Lynx arc presented by Fosbury et al (2003, table 2) is reported. The spectrum shows a relatively large number of line ratios including [OII]/H β and [OIII]/H β in the optical range, reproduced by Fosbury et al by a pure photoionization model with $T_* = 8 \cdot 10^4$ K $\log U = -1$ and $Z = 0.05 Z_\odot$, which was suggested by comparison with synthetic SEDs calculated by STARBURST99 (Leitherer et al 1999). The FWHM of the profiles are ≤ 100 km s $^{-1}$ for lines in the optical and higher for those in the UV. We searched by modelling the spectrum for a (hidden) AGN, but AGN dominated models lead to HeII/H $\beta \geq 1$, higher by a factor ≥ 10 than observed. The shock dominated model MF0 (Table 6, col. 12) calculated by a relatively high shock velocity (320 km s $^{-1}$) and high preshock density ($n_0 = 2000$ cm $^{-3}$) fits most of the UV line ratios but underpredicts [OIII] 5007+/H β by a factor ≥ 10 . A SB radiation dominated model MFSB, calculated by $T_* = 1.1 \cdot 10^5$ K, $U = 0.3$, $D = 4.9 \cdot 10^{20}$ cm, $V_s = 100$ km s $^{-1}$, $n_0 = 300$ cm $^{-3}$ and O/H ~ 0.5 solar, reproduces satisfactorily most of the line ratios from relatively low ionization levels. Model MFSB which accounts for photoionization by a SB + shocks represents gas ejected outwards, while for model MF0 the direction of the emitting gas is ambiguous.

Finally, we show in Figs. 6 and 7 the profiles of the physical parameters throughout the emitting nebula for models MF0 and MFSB, respectively, in order to understand the results. In Figs. 6 and 7 the electron temperature and electron density appear in the top diagrams. In Fig. 7 the nebula is divided into two halves in order to obtain a comparable view at the two edges. Logarithmic

symmetric scales are used for the X-axis. The shock front is on the left of the left panel and the right edge of the right panel is reached by the radiation flux from the SB. In the middle diagrams of Figs. 6 and 7 the fractional abundances of the ions corresponding to significant lines are shown. The bottom diagrams are dedicated to the Ly α /H β , H α /H β and Ly α /H α line ratios (in logarithm). Figs 6 and 7 show that Ly α /H α follows the H $^+$ recombination trend. The two sides of the nebula (shock dominated at the left and radiation dominated at the right of Fig. 7) are bridged by diffuse secondary radiation. In fact, the temperature is $\sim 10^4$ K even in the extended internal region of the nebula. Most of the C, N, O lines come from the radiation dominated side of the nebula.

3.9. Finkelstein et al survey

Finkelstein et al (2011) present in their table 1 the measured line fluxes for a sample of galaxies at $0.24 \leq z \leq 0.324$ by spectroscopy of LAE using the Hectospec spectrograph with the 6 m MMT telescope.

We report in Table 7 the results of modelling the observed line ratios and we add the UV lines NV, CIV and He II consistently calculated by the same models. These lines which are not observed by Finkelstein et al will be discussed in the following. In Table 7 the observed line ratios (EGS7-EGS25, corrected by H α /H $\beta = 3$) are followed in the next rows by the results of SB models (MSB7-MSB25) and AGN models (MAG7-MAG25). The input parameters are reported in Tables 8 and 9).

Ly α lines are calculated consistently with the other lines. Ly α /H β calculated line ratios (col. 3) reproduce the data within a factor of 2. In col. 4 the SFR are indicated for each galaxy. The percentage uncertainty appears in col. 5. The galaxies in the Finkelstein et al sample present rather homogeneous characteristics. The O/H relative abundances are at most solar while the N/H ratios are lower than solar by a factor < 10 . Densities and velocities are relatively low. The flux from the active nucleus is in the range of that found in low luminosity AGNs. The temperature of the stars does not show the maxima corresponding to outbursts (Contini 2014b). The geometrical thickness of the clouds shows that fragmentation is present in the SB neighbourhood rather than in AGNs.

Table 7. Modelling the corrected line ratios to H β = 1 observed by Finkelstein et al (2011)

ID	z	SFR M $_{\odot}$ yr $^{-1}$	Ly α 1215	%	NV 1240	CIV 1550	HeII 1640	[OII] 3727+	[OIII] 5007+	H α 6563	[NII] 6584
EGS7	0.2440	0.4	17.53	15.9	-	-	-	2.14	5.65	3.	0.134
MSB7			24.3	-	0.0014	0.34	0.078	2.3	5.6	2.93	0.16
MAG7			28.6	-	0.0009	0.15	1.22	2.	6.4	3.3	0.18
EGS8*	0.2395	0.035	16.7	32.8	-	-	-	2.47	3.7	3.	<0.03
MSB8			23.8	-	0.0024	0.28	0.0037	2.	3.5	2.95	0.1
MAG8			28.6	-	0.0005	0.14	0.89	2.	3.46	3.34	0.1
EGS10	0.2466	0.12	33.9	16.7	-	-	-	3.06	4.37	3.	<0.06
MSB10			24.6	-	0.016	0.46	0.044	3.2	4.5	2.94	0.12
MAG10			28.	-	0.001	0.029	1.1	3.1	4.65	3.2	0.14
EGS11	0.2524	0.059	41.1	35.3	-	-	-	2.78	1.53	3.	0.84
MSB11			24.5	-	0.1	0.3	0.0026	2.3	1.5	2.96	0.87
MAG11			26.5	-	0.0027	0.1	0.67	2.5	1.57	3.3	0.9
EGS12	0.2515	0.062	48.7	20.8	-	-	-	2.8	2.7	3.	0.38
MSB12			24.5	-	0.067	0.42	0.01	2.9	2.63	3.	0.46
MAG12			28.	-	0.0027	0.28	0.8	2.5	2.8	3.3	0.37
EGS13	0.2607	0.46	17.96	21.	-	-	-	2.8	2.26	3.	0.43
MSB13			24.5	-	0.067	0.42	0.0092	2.9	2.45	2.95	0.47
MAG13			31.54	-	0.017	0.25	0.73	3.	2.35	3.3	0.46
EGS19	0.2666	0.11	33.96	21.9	-	-	-	2.4	1.23	3.	0.86
MSB19			24.4	-	0.1	0.31	0.0046	2.36	1.3	3.	0.86
MAG19			26.4	-	0.0027	0.1	0.61	2.5	1.25	3.	0.96
EGS20*	0.2680	0.073	11.57	27.2	-	-	-	3.04	4.2	2.9	<0.137
MSB20			24.3	-	0.024	0.46	0.015	2.96	4.12	2.93	0.14
MAG20			28.	-	0.001	0.29	1.1	3.	4.5	3.	0.14
EGS21	0.2814	0.06	46.4	21.6	-	-	-	1.98	0.415	3.	0.12-1.4
MSB21			32.	-	0.063	0.155	0.0015	2.2-1.8	0.47-0.4	3.3	0.13-1.2
MAG21a			30.5	-	0.002	0.3	0.27	1.8	0.45	3.46	1.5
MAG21b			28.3	-	0.0027	0.14	0.31	2.1	0.42	3.4	0.15
EGS22	0.2828	0.12	242.	35.9	-	-	-	3.17	0.74	3.	<0.14
MSB22			25.5	-	0.023	0.9	0.011	3.	0.75	2.96	0.13
MAG22			27.9	-	0.002	0.22	0.5	3.2	0.72	3.3	0.12
EGS23	0.2865	0.42	18.4	15.8	-	-	-	2.65	3.7	3.	0.32
MSB23			24.2	-	0.045	0.55	0.012	2.65	3.74	2.93	0.31
MAG23			27.1	-	0.004	0.3	1.0	2.60	3.88	3.2	0.37
EGS25	0.3243	1.06	6.5	16.6	-	-	-	1.76	5.94	3.	0.16
MSB25			24.	-	0.04	0.68	0.023	1.8	6.2	2.93	0.15
MAG25			28.9	-	0.0005	0.11	1.13	1.8	5.95	3.3	0.14

* not Balmer corrected because the observed H α / H β \sim 3.

Table 8. Input parameters for Finkelstein et al. MSB models

model	V $_s$	n $_0$	T $_e$	U	N/H	O/H	D	H β
	1	2	3	4	5	6	7	8
MSB7	100	100	6.4	0.02	0.1	5.	9.	0.02
MSB8	100	100	4.2	0.03	0.2	6.6	3.	0.0196
MSB10	150	100	5.9	0.02	0.1	6.0	4.	0.019
MSB11	150	100	4.	0.03	0.9	6.6	4.	0.027
MSB12	180	100	4.8	0.025	0.4	6.6	5.	0.024
MSB13	180	100	4.7	0.025	0.4	6.6	5.	0.025
MSB19	210	100	3.9	0.04	0.8	6.6	5.	0.038
MSB20	220	100	4.8	0.035	0.13	6.6	1.	0.029
MSB21	170	100	4.	0.015	0.1	6.6	300	0.058
MSB22	200	150	4.2	0.015	0.06	5.2	80	0.023
MSB23	190	100	4.4	0.034	0.2	5.6	1.	0.022
MSB25	170	100	4.9	0.034	0.15	5.	1.	0.023

1: in km s $^{-1}$; 2: in cm $^{-3}$; 3: in 10 4 K; 4: -; 5: in 10 $^{-4}$; 6: in 10 $^{-4}$; 7: in 10 17 cm $^{-2}$; 8: in erg cm $^{-2}$ s $^{-1}$

Table 9. Input parameters for Finkelstein et al. MAG models

model	z	V $_s$	n $_0$	F	N/H	O/H	D	H β
		1	2	3	4	5	6	7
MAG7	0.2440	100	150	7.	0.2	5.6	3	0.066
MAG8	0.2395	100	150	3.	0.1	5.6	3	0.064
MAG10	0.2466	100	150	3.	0.1	6.6	3	0.029
MAG11	0.2524	100	150	1.4	0.8	6.6	3	0.072
MAG12	0.2515	100	150	2.5	0.3	6.0	1.4	0.03
MAG13	0.2607	120	150	2.6	0.3	6.0	1.9	0.045
MAG19	0.2666	100	150	1.2	0.8	6.6	3	0.072
MAG20	0.2680	100	150	2.9	0.1	6.6	1	0.03
MAG21a	0.2814	100	150	0.77	0.2	6.6	1.6	0.026
MAG21b	0.2814	110	150	0.8	0.15	6.6	4	0.068
MAG22	0.2828	110	150	0.86	0.08	6.0	4	0.045
MAG23	0.2865	100	100	1.8	0.3	6.6	2	0.018
MAG25	0.3243	100	150	6.	0.15	5.8	4	0.086

1: in km s $^{-1}$; 2: in cm $^{-3}$; 3: in 10 9 photons cm $^{-2}$ s $^{-1}$ eV $^{-1}$ at the Lyman limit; 4: in 10 $^{-4}$; 5: in 10 $^{-4}$; 6: in 10 19 cm $^{-2}$; 7: in erg cm $^{-2}$ s $^{-1}$

3.10. Predicted Ly α and UV lines from galaxies at 0.06 < z < 0.9

The R $_{[OIII]}$ ([OIII]5007+/[OIII]4363) line ratios indicate that gas densities and temperatures in ranges larger than those deduced in average from the observations should be accounted for. This is valid for the AGN NLR spectra (see e.g. (Contini & Aldrovandi 1986, fig. 4 and references therein, etc.) and for most of the objects throughout the galactic medium (such as SNR, novae,

symbiotic stars) and the extra-galactic one. In Seyfert type 1 galaxies [OIII] lines from the BLR are collisionally deexcited. In Seyfert type 2 the [OIII] lines correspond to gas at V $_s$ = 300-500 km s $^{-1}$ and densities of 10 4 -10 5 cm $^{-3}$. In intermediate type galaxies R $_{[OIII]}$ ranges between high (> 100) and low values (< 20). LINERs (Heckman 1980, Ferland & Netzer 1983, Ho et al 1993) cannot be considered as a low F case (Contini & Aldrovandi 1983, fig. 3). Problems can be solved by adding shock wave hy-

Table 10. The data observed by Ly et al (2014)

ID	zspec	FWHM km s ⁻¹	[OII] 3727+	H β 4861	[OIII] 4363	[OIII] 5007+	H α 6563	[NII] 6583	log([OII]/H β)	log([OIII]5007+/H β)	log(R _(OIII))
MMT01	0.6380	220.0	10.58	9.21	2.25	73.32	0.00	0.00	0.184 ^{0.195} _{0.174}	0.886 ^{0.082} _{0.065}	1.462 ^{0.211} _{0.226}
MMT02	0.4327	247.0	18.20	5.76	0.60	25.83	0.00	0.00	0.621 ^{0.287} _{0.173}	0.644 ^{0.040} _{0.044}	1.549 ^{0.282} _{0.394}
MMT03	0.4809	256.4	20.40	5.81	0.95	12.23	0.00	0.00	0.735 ^{0.211} _{0.200}	0.339 ^{0.052} _{0.049}	1.086 ^{0.269} _{0.129}
MMT04	0.3933	248.6	49.30	21.70	1.38	130.05	0.00	0.00	0.355 ^{0.026} _{0.009}	0.774 ^{0.007} _{0.008}	1.950 ^{0.129} _{0.141}
MMT05	0.3846	232.1	3.70	7.02	1.29	57.92	0.00	0.00	-0.266 ^{0.147} _{0.102}	0.921 ^{0.029} _{0.034}	1.659 ^{0.158} _{0.192}
MMT06	0.3995	260.2	21.33	6.04	0.83	21.97	0.00	0.00	0.734 ^{0.069} _{0.061}	0.543 ^{0.054} _{0.051}	1.319 ^{0.255} _{0.408}
MMT07	0.3896	238.0	19.84	20.84	2.25	153.87	0.00	0.00	0.102 ^{0.166} _{0.129}	0.872 ^{0.008} _{0.007}	1.777 ^{0.132} _{0.123}
MMT08	0.6335	239.4	27.33	10.90	1.88	42.30	0.00	0.00	0.613 ^{0.355} _{0.269}	0.584 ^{0.100} _{0.096}	1.260 ^{0.332} _{0.411}
MMT09	0.4788	235.2	16.74	6.82	1.49	39.48	0.00	0.00	0.585 ^{0.127} _{0.044}	0.762 ^{0.093} _{0.088}	1.338 ^{0.261} _{0.270}
MMT10	0.0683	286.1	22.46	18.19	2.02	121.87	59.04	1.26	0.144 ^{0.056} _{0.039}	0.824 ^{0.021} _{0.024}	1.717 ^{0.335} _{0.157}
MMT11	0.1752	276.9	42.42	22.01	2.05	144.89	78.37	3.13	0.386 ^{0.034} _{0.034}	0.823 ^{0.024} _{0.021}	1.803 ^{0.157} _{0.209}
MMT12	0.6405	214.5	23.57	6.18	1.31	40.13	0.00	0.00	0.840 ^{0.601} _{0.360}	0.812 ^{0.131} _{0.119}	1.318 ^{0.439} _{0.542}
MMT13	0.4696	209.1	6.03	6.51	1.15	39.59	0.00	0.00	0.072 ^{0.231} _{0.160}	0.780 ^{0.034} _{0.037}	1.524 ^{0.268} _{0.307}
MMT14	0.4644	280.6	100.27	56.75	2.01	354.12	0.00	0.00	0.266 ^{0.033} _{0.019}	0.794 ^{0.005} _{0.005}	2.215 ^{0.112} _{0.150}
Keck1	0.8390	124.6	4.62	7.80	0.80	61.10	0.00	0.00	-0.016 ^{0.060} _{0.081}	0.897 ^{0.011} _{0.010}	1.811 ^{0.091} _{0.094}
Keck2	0.6230	89.5	3.49	2.33	0.67	17.60	0.00	0.00	0.144 ^{0.041} _{0.040}	0.843 ^{0.019} _{0.021}	1.440 ^{0.134} _{0.148}
Keck3	0.7906	121.2	27.88	12.50	0.27	59.17	0.00	0.00	0.658 ^{0.038} _{0.042}	0.676 ^{0.008} _{0.007}	2.142 ^{0.162} _{0.224}
Keck4	0.8829	178.5	13.77	7.28	0.33	35.60	0.00	0.00	0.275 ^{0.017} _{0.017}	0.683 ^{0.014} _{0.014}	2.018 ^{0.235} _{0.290}
Keck5	0.8353	101.1	1.85	1.10	0.58	7.99	0.00	0.00	0.362 ^{0.216} _{0.163}	0.879 ^{0.035} _{0.035}	1.102 ^{0.252} _{0.267}
Keck6	0.8237	90.5	0.05	0.88	0.19	5.36	0.00	0.00	-1.010 ^{0.595} _{0.937}	0.770 ^{0.031} _{0.030}	1.346 ^{0.281} _{0.320}

Note : the line fluxes are in 10^{-17} erg cm⁻² s⁻¹ with 68 % confidence uncertainties

drodynamics to the calculations of the spectra (Contini 1997 and references therein) or by assuming a density gradient or a stratification of emitting filaments (Pequignot 1984, Filippenko 1984, etc.) The importance of the [OIII]4363 line recently emerged for high z galaxies, because constraining the models. To cross-check this issue we calculate the Ly α /H β line ratios for galaxies which show spectra constrained by the [OIII] 4363 line (see Contini 2014a, Ly et al.2014). We choose the Ly et al (2014) survey because the reddening corrected spectra contain [OIII]5007+4959, [OIII] 4363, [OII] 3727, H β and H α lines.

In Table 10 the results of Ly et al. (2014) observations obtained by the Subaru telescope are reported. We compare the calculated with observed line ratios in Table 11. The uncertainty for model calculations is about 10 %.

In Table 12 models m1-m20 are calculated by SB dominated (+shock) models, while models mpl1-mpl20 (described in Table 13) are calculated by AGN (+shocks) dominated models. Table 11 show that [OII]/H β and [OIII]/H β line ratios are well fitted by both SB and AGN models, but, regarding the [OIII]5007+/[OIII]4363 line ratios, the SB dominated models fit the data of nearly all galaxies, while MMT5, MMT12, and Keck3 are better reproduced by AGN dominated models. For MMT4, Keck4 and Keck6 the SB and AGN photoionizing models act with similar weights.

The [OIII]4363/H β is the key line ratio for choosing between SB or AGN dominated models. Indeed the shock plays an important role, but the effect of photoionization cannot be neglected. The ionization parameter (U) and the SB effective temperature (T_*) for SB and the power-law flux from the AGN are determined by fitting the [OIII]5007+/H β and [OII]3727/H β line ratios. With those input parameters, the [OIII]4363/H β line ratios for SB are higher by factors very roughly ~ 10 than those calculated for the AGNs, indicating that the shock effect is relatively strong. So [OIII]5007+/[OIII]4363 are lower for starbursts.

The densities in the downstream emitting regions are higher by a factor of ~ 10 , depending on V_s . Regarding the [NII]/H β line ratios, the H α /H β line ratios for MMT10 and MMT11 are roughly between 3 and 4, the [NII]/H β line ratios were directly calculated. The result of N/H is given only for the

SB dominated models which well reproduce all the other line ratios. We obtained low N/H relative abundances ($0.25 \cdot 10^{-4}$) for the two galaxies MMT10 and MMT11. The results for O/H (in 10^{-4} units) are shown in Tables 12 and 13. O/H relative abundances calculated by detailed modelling are closer to solar and higher than those calculated by direct methods.

4. Discussion and concluding remarks

In previous sections we have been investigating the gas physical conditions and element abundances in galaxies at relatively high z , selected by their characteristic line spectra, i.e. including the Ly α line and the lines which constrain the models. A detailed modelling process has been used. All the models are calculated at the emitting nebulae in the different galaxies. They lead to Ly α /H β higher than observed, except for some SB dominated models, MDS (Table 4), MV1 and MV6 (Table 5) and some models in the Finkelstein et al survey (Tables 7-9). The models best reproducing the data in Tables 2-6 show that most of the spectra are fitted by the summed contributions of two types : those emitted from the high velocity (~ 700 -1500 km s⁻¹) clouds (generally close to an AGN), which explain the high ionization level lines and UV - X-ray data in the continuum SED, and those emitted from the relatively low V_s (~ 100 -300 km s⁻¹), n_0 (100 -300 cm⁻³) radiation dominated clouds (by a AGN or a SB) which confirm the narrow optical line profiles, as well as the optical spectral and continuum data. In some cases one or more model components show that the photoionizing flux from the active source is prevented from reaching the gas, or that the source is absent. Therefore, the clouds within the galaxies are ionized and heated only by the shock. In the HDF galaxy (Dawson et al) the high V_s (1300 km s⁻¹) clouds are found in the surroundings of a SB corresponding to a high T_* . In the BX418 galaxy (Erb et al), the high velocity gas ($V_s = 600$ -800 km s⁻¹) shows a preshock density higher by a factor > 10 than in the other objects. The shock velocities were most probably reduced by collision with high density gas. These clouds are located in the surroundings of an AGN. This is valid also for the shock dominated clouds (model MF0, Table 6) in the Lynx arc (Fosbury et al). A few

Table 11. Modelling the corrected line ratios to $H\beta = 1$ observed by Ly et al. (2014)

ID	OVI 1034	OV 1215	Ly α 1215	NV 1240	CIV 1549	HeII 1640	[OII] 3727+	[OIII] 4363	[OIII] 5007+
MMT01	-	-	-	-	-	-	1.53	0.26	7.69
m1	38.7	7.86	25.89	3.	7.82	0.26	1.53	0.26	7.69
mpl1	5.3	1.11	32.	0.43	0.68	1.45	1.5	0.05	7.8
MMT02	-	-	-	-	-	-	4.18	0.124	4.4
m2	57.8	10.6	26.2	3.75	9.7	0.14	3.9	0.23	4.2
mpl2	5.	1.	30.9	0.39	0.98	1.44	4.	0.035	4.74
MMT03	-	-	-	-	-	-	5.43	0.18	2.18
m3	54.9	10.9	36.7	4.2	10.9	0.117	5.2	0.2	2.5
mpl3	10.3	1.93	30.8	0.65	1.64	1.15	5.	0.04	2.4
MMT04	-	-	-	-	-	-	2.26	0.07	5.94
m4	46.8	9.	26.	3.65	9.28	0.18	2.7	0.2	5.43
mpl4	2.7	0.6	30.7	0.32	0.79	1.78	3.	0.034	5.8
MMT05	-	-	-	-	-	-	0.54	0.18	8.33
m5	3.16	0.67	24.6	0.37	0.96	0.48	0.9	0.04	8.33
mpl5	2.42	0.52	32.2	0.36	0.91	2.11	1.2	0.07	8.4
MMT06	-	-	-	-	-	-	5.42	0.167	3.49
m6	69.4	16.	49.7	13.4	30	0.425	6.	0.25	3.1
mpl6	8.3	1.52	30.5	0.51	1.31	1.29	5.1	0.038	3.5
MMT07	-	-	-	-	-	-	1.26	0.12	7.44
m7	36.7	7.74	26.	3.45	8.73	0.3	1.35	0.19	7.33
mpl7	5.3	1.11	32.	0.43	0.68	1.65	1.4	0.05	7.8
MMT08	-	-	-	-	-	-	4.1	0.21	3.84
m8	57.5	10.5	26.	3.73	9.61	0.14	4.	0.226	3.94
mpl8	6.65	1.3	30.9	0.5	1.25	1.28	4.4	0.036	3.88
MMT09	-	-	-	-	-	-	3.84	0.265	5.78
m9	59.2	11.1	26.2	4.2	10.8	0.18	3.5	0.264	5.9
mpl9	4.1	0.83	31.2	0.37	0.92	1.66	3.71	0.04	5.75
MMT10	-	-	-	-	-	-	1.39	0.128	6.67
m10	26.8	6.35	25.9	0.86	8.75	0.23	1.41	0.16	6.42
mpl10	7.	1.38	32.3	0.54	0.58	1.54	1.3	0.04	6.5
MMT11	-	-	-	-	-	-	2.43	0.1	6.65
m11	30.5	6.63	25.6	0.63	6.75	0.123	2.	0.167	6.0
mpl11	2.66	0.52	32.8	0.21	0.53	1.43	2.3	0.04	6.3
MMT12	-	-	-	-	-	-	6.9	0.31	6.5
m12	118.7	21.8	27.8	7.7	19.8	0.27	6.7	0.45	6.2
mpl12	57.6	20.4	27.1	3.	8.2	1.17	6.2	0.28	6.4
MMT13	-	-	-	-	-	-	1.18	0.18	6.03
m13	26.	6.25	25.9	0.9	9.12	0.21	1.39	0.15	6.0
mpl13	4.74	1.04	32.3	0.47	1.23	1.53	1.2	0.055	6.28
MMT14	-	-	-	-	-	-	1.85	0.04	6.22
m14	72.4	17.	28.3	3.12	30.3	0.38	2.4	0.2	6.1
mpl14	4.64	1.17	26.45	1.47	3.3	2.55	1.8	0.059	6.1
Keck1	-	-	-	-	-	-	0.96	0.12	7.89
m15	28.9	6.3	25.8	2.8	7.25	0.47	0.9	0.16	7.8
mpl15	2.4	0.52	32.4	0.36	0.9	2.02	1.2	0.063	7.88
Keck2	-	-	-	-	-	-	1.39	0.25	6.97
m16	0.	0.02	24.3	0.043	10.9	0.165	1.3	0.29	6.7
mpl16	1.41	0.33	34.9	0.23	0.59	1.96	1.27	0.05	7.
Keck3	-	-	-	-	-	-	4.55	0.034	4.74
m17	13.6	10.4	27.4	4.12	12.9	0.07	4.	0.32	4.57
mpl17	0.081	0.3	26.4	0.42	1.81	1.55	4.4	0.049	4.75
Keck4	-	-	-	-	-	-	1.88	0.046	4.82
m18	10.7	2.2	24.9	0.68	1.78	0.047	1.8	0.057	4.8
mpl18	2.45	0.54	35.	0.3	0.72	2.57	1.6	0.035	5.0
Keck5	-	-	-	-	-	-	2.3	0.6	7.56
m19	0.003	0.3	27.3	0.74	20.7	0.15	2.5	0.45	8.
mpl19	0.03	0.095	34.4	0.14	0.64	1.95	2.1	0.05	7.6
Keck20	-	-	-	-	-	-	0.096	0.27	5.9
m20	0.	0.03	23.8	0.07	14.0	3.72	0.11	0.15	6.4
mpl20	420.	190.	38.	85.	22.5	7.9	0.08	0.43	6.

galaxies from the radio survey of Humphrey et al (Table 3) do not show the high V_s component which is neither present in the galaxies selected from the Vernet et al survey (Table 5). Here, the clouds are characterised by the very low V_s and n_0 , similar or lower than those calculated to reproduce the Finkelstein et al spectra (Tables 8 and 9).

We report in Fig. 8 HeII 1640/CIV 1549 versus Ly α /CIV 1549 calculated by the models presented in GRID1, considering

gas in the conditions suitable to the NLR of AGN. The line ratios were calculated by GRID1 adopting two different geometrical thickness of the emitting clouds, $D=10^{17}$ cm and 10^{19} cm. In GRID1, for each set of n_0 and V_s a series of models with different F , ($\log F=8,9,10,11,12$) were adopted. $F=0$ represents the shock dominated case and corresponds to the lowest HeII/CIV and Ly α /CIV. Solar (Allen 1976) element abundances were used to calculate the spectra. The HeII/CIV and Ly α /CIV trends (for

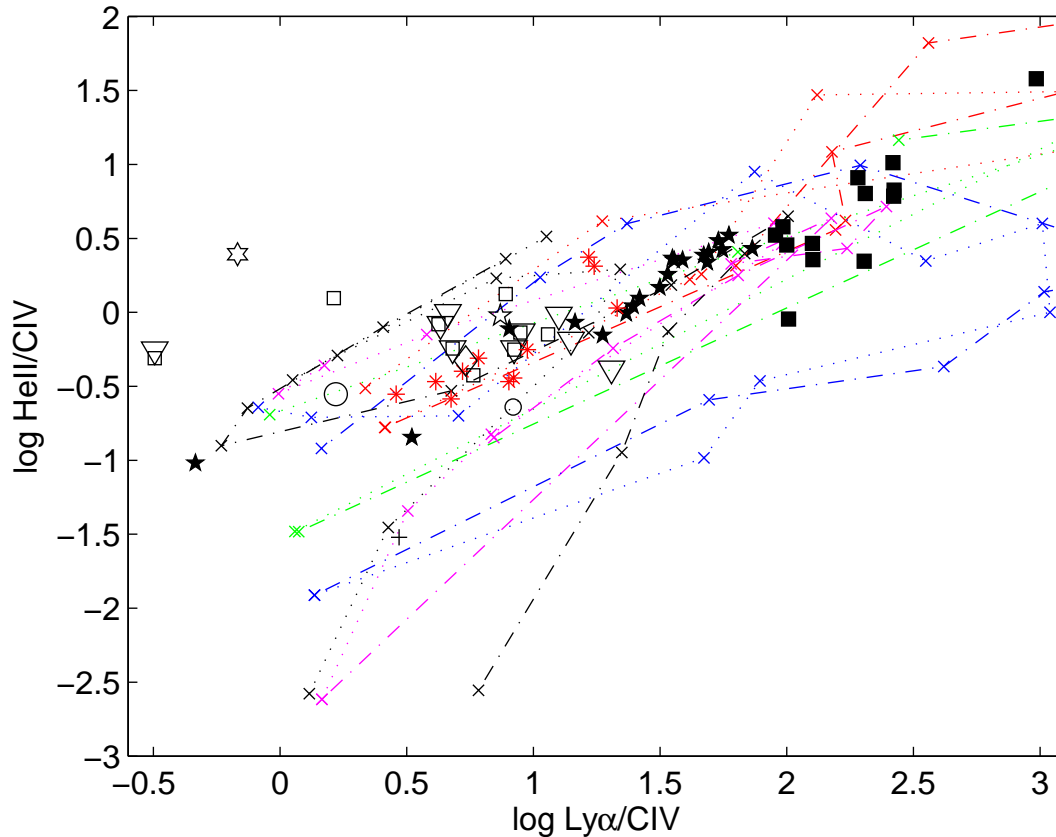


Fig. 8. The HeII/CIV versus Ly/CIV for NLR of AGN. Open circle : Norman et al, hexagon : Dawson et al, diamond : Stern et al, large pentagram : Dey et al; red asterisks : Collins et al., triangles : Vernet et al, open squares : Humphrey et al.; filled pentagrams (small for SB and large for AGN models): Ly et al. ; black filled squares (small for SB and large for AGN models) : Finkelstein et al.; small circle: Erb et al ; plus: Fosbury et al. Line symbols : see Table 1.

each V_s) follow the increasing photoionization flux, because both HeII and Ly α are recombination lines which depend on photoionization, while the fractional abundance distribution of carbon ions in different ionization levels strongly depends on gas temperature and density which are affected by the shock.

The data observed for nearly all the AGN dominated objects are nested between models showing $V_s \sim 100$ and 200 km s^{-1} , the fluxes ranging throughout a large scale, and both geometrically thin and thick clouds. Also shown in Fig. 8 are the spectral data observed from the local galaxy Mrk3 (Collins et al 2005) because they include the Ly α and UV lines. The data (reddening corrected) refer to different regions within the galaxy. The spectra represent average conditions covering small regions within the galaxy. So they tend to show intrinsic conditions of the gas rather than the averaged ones obtained by modelling the observed spectra covering the entire galaxy, as necessarily occurs for high z galaxies. The Mrk3 data are less scattered than those observed from high z galaxies and follow the model trends.

In Fig. 8 we added the data based on the Finkelstein et al and Ly et al. observations. They do not represent observed HeII/CIV versus observed Ly α /CIV, but the calculated line ratios which are strongly constrained by the observed optical lines. Finkelstein et al and Ly et al. objects follow the trends of AGN (+shock) dominated models with roughly constant velocities. The observed line ratios referring to the other galaxies are scat-

tered for different F . The Finkelstein et al and Ly et al samples are situated close to higher shock velocity models.

Finally, in Figs. 9 the physical parameters (V_s , n_0 , T_* , U , F , D), the H α flux at the nebula and O/H and N/H relative abundances calculated for the present sample of galaxies are presented as function of the SFR. SFR were calculated by the H α flux measured at Earth by the observers. We chose H α instead of Ly α because less affected by scattering and absorption problems. For galaxies in which the H α data were not available, we used Ly α and we calculated H α line fluxes by noticing that the Ly α /H β line ratios can be approximated to ~ 25 for many models (Fig. 1) and that H α /H $\beta \sim 3$.

The sample of galaxies which emit Ly α and UV lines do not show peculiar physical conditions of the emitting gas, nor abnormal element abundances. However, for some galaxies of the Humphrey et al, Dawson et al, Stern et al, Dey et al, Norman et al surveys, emitting gas with relatively high V_s ($> 1000 \text{ km s}^{-1}$) is revealed by the complex FWHM of the line profiles. Such velocities are upper limits to those characteristic of the AGN NLR. Generally, higher n_0 accompany higher V_s leading to collisionally deexcited forbidden lines. This is not the case for the Ly α line emitting galaxies modelled throughout this paper. In the Humphrey et al galaxy 0211-122 spectrum reported in Table 2, for instance, [OIII] 5007 lines with FWHM = $1300 \pm 60 \text{ km s}^{-1}$ and [OII] 3727 with FWHM = $730 \pm 160 \text{ km s}^{-1}$ were observed. Most of the high velocity models are shock dominated.

In these cases, the electron temperature and density steeply drop to $T \geq 10^3$ K (Fig. 6) at a certain distance from the shock-front (which depends on V_s) because the primary flux is absent and the secondary one is relatively weak.

The high T_* ($> 10^5$ K) which indicates that the SB stars are close to outburst (Contini 2014b) were found in a few objects (4C+23.56 at $z=2.479$ from the Humphrey et al survey, SST24 at $z=2.858$ from the Dey et al survey and the Lynx arc at $z=3.357$ from Fosbury et al observations) within more than 50 galaxies in the sample. These outstanding temperature, which are characteristic of galaxies showing some activity (Contini 2014b), are isolated events at the state of the art. Considering the evolutionary paths in the H-R diagrams for stars of different mass during the pre-main-sequence phase, these temperatures can be reached by $\geq 9M_\odot$ stars in a lifetime of $\geq 10^5$ years (Prialnik 2000, fig. 8.1), which is very short compared to the redshift z age (> 2 Gyr).

Fig. 9 shows that the SFR between ~ 1 and $\sim 300 M_\odot \text{ yr}^{-1}$ is accompanied by relatively high shock velocities ($> 1000 \text{ km s}^{-1}$), but gaseous cloud densities are relatively low, similar to those in the AGN NLR and in the SB surrounding ($n_0 \leq 350 \text{ cm}^{-3}$) for SFR $\geq 10 M_\odot \text{ yr}^{-1}$. O/H reaches a lower limit minimum for some galaxies at SFR $< 10 M_\odot \text{ yr}^{-1}$, then it grows with SFR to solar values at SFR $\sim 300 M_\odot \text{ yr}^{-1}$. The N/H relative abundances show a large scattering. N/H are particularly low for a few galaxies in the Finkelstein et al survey at $z \sim 0.25$. Humphrey et al, however, claim that nuclear activity and star formation which lead to solar metallicities at early times, are seen through lack of variability and high metallicity between $z=2.5$ and 0. The geometrical thickness of the emitting clouds presents minimum $D \leq 10^{16} \text{ cm}$. D and consequently also H α fluxes calculated at the nebula show a large scattering covering roughly 4 orders of magnitude for SFR between 1 and $650 M_\odot \text{ yr}^{-1}$, indicating fragmentation by turbulence in a shock dominated regime.

Acknowledgements

I am very grateful to the referee for reviewing the paper and for many comments which improved its presentation. I thank Dr. Chun Ly for providing the data in suitable format.

References

- Aldrovandi, S.M.V. & Contini 1994, A&A, 140, 368
Allen, C.W. 1976 Astrophysical Quantities, London: Athlone (3rd edition)
Atek, H.; Kunth, D.; Schaerer, D.; Mas-Hesse, J.; Hayes, M.; stlin, G.; Kneib, J-P, 2014, A&A, 561, 89
Beck, R. 2012, JPhCS, 372, 02051
Bose, S. et al. 2015, arXiv:1504.06207
Charlot, S., Fall, S.M. 1993, ApJ, 415, 580
Cimatti, A., di Serego Alighieri, S., Vernet, J., Cohen, M., Fosbury, R.A.E. 1988, ApJ, 499, L21
Collins, N. R.; Kraemer, S. B.; Crenshaw, D. M.; Ruiz, J.; Deo, R.; Bruhweiler, F. C. 2005, ApJ, 619, 116
Contini, M. 2014a, A&A, 564, 19
Contini, M. 2014b, A&A, 572, 65
Contini, M. 2013a, MNRAS, 429, 242
Contini, M. 2013b, arXiv:1310.5447
Contini, M. 2012, MNRAS, 425, 1205
Contini, M. 2009, MNRAS, 399, 1175
Contini, M. 1997, A&A, 323, 71
Contini, M., Aldrovandi, S.M. 1983, A&A, 127, 15

Table 12. The physical parameters and the relative abundances for Ly et al SB dominated models (m1-m20)

model	V_s ¹	n_0	T_*	U	D	O/H	H β calc
	1	2	3	-	4	5	6
m1	220	120	5.	0.05	8.	6.5	0.00176
m2	260	120	3.8	0.03	8.6	7.3	0.0016
m3	240	130	1.	0.001	8.	6.6	0.0015
m4	260	110	4.7	0.03	10.	6.3	0.0016
m5	250	110	7.	0.06	40.	4.5	0.018
m6	260	130	8.	0.0005	28.	3.	0.0008
m7	220	120	5.1	0.05	8.	5.6	0.0017
m8	260	120	3.7	0.03	8.6	7.3	0.0016
m9	260	110	4.4	0.03	9.5	6.8	0.0013
m10	200	120	5.	0.04	8.	4.7	0.0018
m11	200	120	4.5	0.04	8.	6.6	0.003
m12	260	120	3.6	0.02	7.7	7.3	0.00076
m13	200	120	4.9	0.04	8.	4.4	0.00176
m14	200	120	4.6	0.03	7.	5.5	0.0014
m15	200	120	5.4	0.06	8.	5.5	0.0019
m16	90	120	4.3	0.06	5.	6.6	0.0004
m17	140	120	3.4	0.03	2.8	7.35	0.00064
m18	200	140	4.5	0.04	13.	8.	0.0075
m19	100	120	4.5	0.03	3.	5.5	0.0003
m20	90	100	5.7	0.2	8.	5.5	0.00035

1: in km s^{-1} ; 2: in cm^{-3} ; 3: in 10^4 K ; 4: in 10^{15} cm ; 5: in 10^{-4} ; 6: in $\text{erg cm}^{-2} \text{ s}^{-1}$

Table 13. The physical parameters and the relative abundances for Ly et al AGN dominated models (mpl1-mpl20)

model	V_s	n_0	F	D	O/H	H β calc
	1	2	3	4	5	6
mpl1	220	1000	8	1	6.6	0.124
mpl2	220	370	2	10	6.6	0.048
mpl3	240	330	1	20	7.6	0.025
mpl4	220	320	2.8	30	4.6	0.06
mpl5	280	620	10	3	3.6	0.158
mpl6	250	300	1.2	15	7.6	0.03
mpl7	220	1000	8	1	6.6	0.124
mpl8	240	330	1.5	10	6.6	0.036
mpl9	240	330	2.4	12	5.6	0.053
mpl10	250	1000	7.6	1	6.6	0.11
mpl11	250	550	6	7	6.6	0.15
mpl12	240	160	0.25	5.6	8.9	0.0021
mpl13	220	1000	7.4	1	5.6	0.125
mpl14	250	160	1	12	2	0.01
mpl15	220	780	1.3	4	3.6	0.24
mpl16	220	720	12	4	3.6	0.24
mpl17	120	260	0.6	9	5.	0.114
mpl18	230	720	7.3	4	4.5	0.17
mpl19	120	920	7	4	4.6	0.13
mpl20	90	100	6	2	4.6	0.00005

1: in km s^{-1} ; 2: in cm^{-3} ; 3: in $10^{10} \text{ photons cm}^{-2} \text{ s}^{-1} \text{ eV}^{-1}$ at the Lyman limit; 4: in 10^{15} cm ; 5: in 10^{-4} ; 6: in $\text{erg cm}^{-2} \text{ s}^{-1}$

- Contini, M., Aldrovandi, S.M. 1986, A&A, 168, 41
Contini, M. & Viegas, S.M.A. 2001a, ApJS, 132, 211
Contini, M. & Viegas, S.M.A. 2001b, ApJS, 137, 75
Contini, M., Angeloni, R., Rafanelli, P. 2009, A&A, 496, 759
Contini, M., Cracco, V., Ciroti, S., & La Mura, G. 2012, A&A, 545, A72
Contini, M., Viegas, S.M., Prieto, M.A. 2004, MNRAS, 348, 1065
Cox, D.P. 1972, ApJ, 178, 143
Crenshaw, D.M. et al 2002, ApJ, 566, 187
Dawson, S.; McCrady, N.; Stern, D.; Eckart, M. E.; Spinrad, H.; Liu, M. C.; Graham, J. R. 2003, AJ, 125, 1236
Dey, A. et al. 2005, ApJ, 629, 654
Dwek, E. 1981, ApJ, 247, 614
Erb, D.K., Pettini, M., Shapley, A.E., Steidel, C.C., Law, D.R., Naveen, A.R. 2010, ApJ, 719, 1168
Ferland, G., Netzer, H. 1983, ApJ, 264, 105

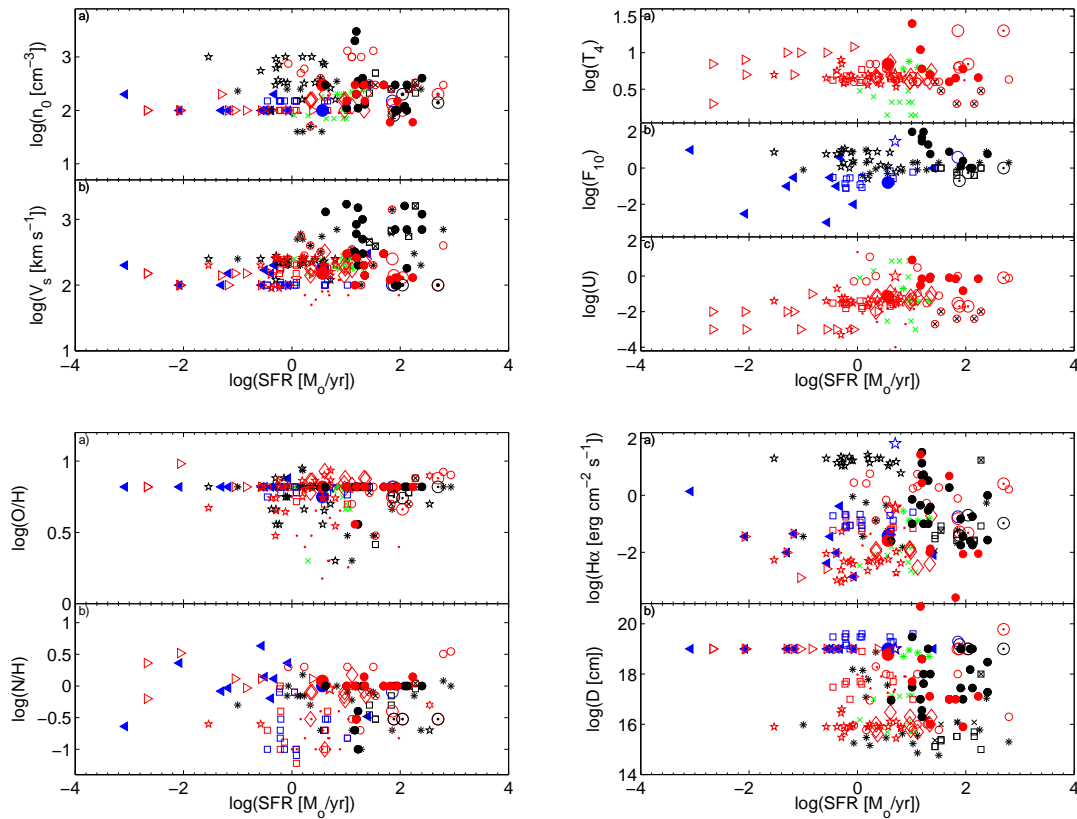


Fig. 9. The physical parameters calculated for the galaxy surveys as a function of the SFR. Symbols as in Contini 2014a, fig. 5. For the present sample : blue open squares : Finkelstein et al for AGN; red open squares : Finkelstein et al. for SB. The results for Ly et al (2014) data are represented by pentagrams, red for starbursts and black for AGN; black filled circles: Dey et al., Dawson et al., Norman et al., Stern et al., Humphrey et al., Vernet et al., Erb et al, and Fosbury et al. AGN models; red filled circles : the same for SB dominated models.

Field, G.B., Steigman, G. 1971, ApJ, 166, 59
Filippenko, A.V. 1985, ApJ, 289, 475
Finkelstein, S. L.; Cohen, S. H.; Moustakas, J.; Malhotra, S., Rhoads, J.E.; Papovich, C. 2011, ApJ, 733, 117
Fosbury, R.A.E. et al 2003, ApJ, 596, 797
Hamann, F. & Ferland, G. 1993, ApJ, 418, 11
Heckman, T.M. 1980 A&A, 87, 152
Heng, K., Sunyaev, R.A. 2008, A&A, 481, 117
Ho, L.C., Filippenko, A.V., Sargent, W.I.W. 1993, ApJ, 417, 63
Humphrey, A.; Villar-Martin, M.; Vernet, J.; Fosbury, R.; di Serego Alighieri, S.; Binette, L. 2008, MNRAS, 383, 11
Knopp, G.P. & Chambers, K.C. 1997, ApJS, 109, 367
Ly, C.; Malkan, M. A.; Nagao, T.; Kashikawa, N.; Shimasaku, K.; Hayashi, M. 2014, ApJS, 780, 122
Norman, C. et al 2002, ApJ, 571, 218
Osterbrock, D.E. Astrophysics of Gaseous Nebulae and Active Galactic Nuclei. Mill Valley, CA: University Science Books; 1989.
Oteo, I. et al. 2012, A&A, 541, 650
Pequignot, D. 1984, A&A, 131, 159
Prialnik, D. 2000 in An Introduction to the Theory of Stellar Structure and Evolution, Cambridge University Press
Richards, E.A. 2000, ApJ, 533, 611
Rodríguez-Ardila, A., Contini, M., Viegas, S.M. 2005, MNRAS, 357, 220
Ryan Jr., R.E., Cohen, S.H., Windhorst, R.A., Silk, J. 2008, ApJ, 678, 751

Stanford, S.A., Elston, R., Eisenhardt, P., R., M., Spinrad, H., Stern, D., Dey, A. 1997, AJ, 114, 2232
Steigman, G., Werner, M.W., Geldon, F.M. 1971, ApJ, 168, 373
Stern, D. et al. 2002, ApJ, 568, 71
Turner, T.J. et al 2001, ApJ, 561, 131
Vernet, J.; Fosbury, R. A. E.; Villar-Martin, M.; Cohen, M. H.; Cimatti, A.; di Serego Alighieri, S.; Goodrich, R. W. 2001, A&A, 366, 7
White, H.E., 1934, Introduction to Atomic Spectra, McGROW-HILL book company, New York and London.
Williams, R.E. 1967, ApJ, 147, 552
Yajima, H., Li, Y., Zhu, Q. 2012 arXiv:1210.6440